TOI-6695: a pair of near-resonant massive planets observed with TESS from the WINE survey

Eberhardt, J.; Trifonov, T.; Henning, T.; Tala Pinto, M.; Brahm, R.; Jordán, A.; ... ; Winn, J.N.

The Astronomical Journal, 169:298 (19pp), 2025 June https://doi.org/10.3847/1538-3881/adc44e

TOI-6695: A Pair of Near-resonant Massive Planets Observed with TESS from the WINE Survey*

Jan Eberhardt[1], Trifon Trifonov[1,2,3], Thomas Henning[1], Marcelo Tala Pinto[4], Rafael Brahm[4,5], Andrés Jordán[4,5], Nestor Espinoza[6], Matías I. Jones[7], Melissa J. Hobson[8], Felipe I. Rojas[5,9], Martin Schlecker[1,10], Lorena Acuña[1], Remo Burn[1], Gavin Boyle[11,12], Rodrigo Leiva[5,13], James McCormac[14], Nicholas Dunckel[11], Diana Dragomir[15], Jeffrey D. Crane[16], Stephen Shectman[16], Johanna K. Teske[16,17], David Osip[18], Arvind F. Gupta[19], Solène Ulmer-Moll[8,20], François Bouchy[8], Monika Lendl[8], Davide Gandolfi[21], George R. Ricker[22], Jon M. Jenkins[23], Sara Seager[22,24,25], and Joshua N. Winn[26]

[1] Max-Planck-Institut für Astronomie, Königstuhl 17, 69117 Heidelberg, Germany
[2] Departmentof Astronomy, Sofia University "St Kliment Ohridski," 5 James Bourchier Boulevard, BG-1164 Sofia, Bulgaria
[3] Landessternwarte, Zentrum für Astronomie der Universität Heidelberg, Königstuhl 12, 69117 Heidelberg, Germany
[4] Facultad de Ingeniera y Ciencias, Universidad Adolfo Ibáñez, Av. Diagonal las Torres 2640, Peñalolén, Santiago, Chile
[5] Millennium Institute for Astrophysics, Chile
[6] Space Telescope Science Institute, 3700 San Martin Drive, Baltimore, MD 21218, USA
[7] European Southern Observatory, Alonso de Córdova 3107, Vitacura, Casilla 19001, Santiago, Chile
[8] Observatoire de Genève, Département d'Astronomie, Université de Genève, Chemin Pegasi 51b, 1290 Versoix, Switzerland
[9] Instituto de Astrofísica, Facultad de Física, Pontificia Universidad Católica de Chile, Chile
[10] Department of Astronomy/Steward Observatory, The University of Arizona, 933 North Cherry Avenue, Tucson, AZ 85721, USA
[11] El Sauce Observatory, Coquimbo Province, Chile
[12] Cavendish Laboratory, J J Thomson Avenue, Cambridge, CB3 0HE, UK
[13] Instituto de astrofísica de Andalucía, CSIC, Glorieta de la Astronomía s/n, 18008 Granada, Spain
[14] Department of Physics, University of Warwick, Gibbet Hill Road, Coventry, CV4 7AL, UK
[15] Department of Physics and Astronomy, University of New Mexico, 210 Yale Boulevard, Albuquerque, NM 87131, USA
[16] The Observatories of the Carnegie Institution for Science, 813 Santa Barbara Street, Pasadena, CA 91101, USA
[17] Earth and Planets Laboratory, Carnegie Institution for Science, 5241 Broad Branch Road, NW, Washington, DC 20015, USA
[18] Carnegie Science—Las Campanas Observatory, Chile
[19] U.S. National Science Foundation National Optical-Infrared Astronomy Research Laboratory, 950 N. Cherry Avenue, Tucson, AZ 85719, USA
[20] Leiden Observatory, Leiden University, P.O. Box 9513, 2300 RA Leiden, The Netherlands
[21] Dipartimento di Fisica, Università degli Studi di Torino, Via Pietro Giuria, 1, 10125 Torino, Italy
[22] Department of Physics and Kavli Institute for Astrophysics and Space Research, Massachusetts Institute of Technology, Cambridge, MA 02139, USA
[23] NASA Ames Research Center, Moffett Field, CA 94035, USA
[24] Department of Earth, Atmospheric and Planetary Sciences, Massachusetts Institute of Technology, Cambridge, MA 02139, USA
[25] Department of Aeronautics and Astronautics, MIT, 77 Massachusetts Avenue, Cambridge, MA 02139, USA
[26] Department of Astrophysical Sciences, Princeton University, NJ 08544, USA
Received 2025 January 13; revised 2025 March 21; accepted 2025 March 22; published 2025 May 8

Abstract

We present the discovery and characterization of a pair of warm Jovian-mass exoplanets orbiting the Sun-like star TOI-6695, based on Transiting Exoplanet Survey Satellite (TESS) transits and precise radial velocity (RV) measurements obtained with FEROS, HARPS, CHIRON, CORALIE, and PFS. The transiting exoplanet TOI-6695b has an orbital period of ∼80.4 days, a radius of $0.85R_{\rm jup}$, and a mass of $0.21M_{\rm jup}$. The outer planet has a minimum mass of $1.45M_{\rm jup}$ and an orbital period of about 242.4 days, confidently constrained by the Doppler time-series data. The TOI-6695 exoplanet system exhibits transit-timing variations due to the dynamical interaction of the planets, which reside near a 3:1 mean-motion resonance. We modeled the TOI-6695 system's orbital and dynamical configuration by performing self-consistent *N*-body fits of TESS photometry, ground-based photometry from Observatoire Moana, and precise RV data, all of which are consistent with the presence of a warm Jovian-mass duo of exoplanets.

Unified Astronomy Thesaurus concepts: Exoplanet astronomy (486); Radial velocity (1332); Transit photometry (1709); Exoplanet detection methods (489)

1. Introduction

The first discovery of an exoplanet around a solar-type star by M. Mayor & D. Queloz (1995) using radial velocity (RV) measurements marked one of the major milestones in modern astronomy and astrophysics. Since the discovery of the hot Jupiter 51 Peg b in 1995, the field of exoplanetary science progressed rapidly, revealing over 5800 known exoplanets,[27] discovered with a variety of astronomical techniques, such as Doppler RV measurements, transit photometry (e.g.,

* Based on observations collected at the European Organization for Astronomical Research in the Southern Hemisphere under MPG programmes 0100.A-9007(A), 0104.A-9007(A), 0108.A-9003(A), 0109.A-9003(A), 105.20GX.001 (PI Brahm), 105.20L0.001 (PI Bouchy), 106.21ER.001 (PI Brahm),106.21TJ.001 (PI Gandolfi), 108.22A8.001 (PI Brahm), 109.239V.001 (PI Brahm), 110.23YQ.001 (PI Brahm), and 112.25W1.001 (PI Brahm). This paper includes data gathered with the 6.5 m Magellan Telescopes located at Las Campanas Observatory, Chile.

[27] https://exoplanetarchive.ipac.caltech.edu/; 2024 December 16.

HD 209458; D. Charbonneau et al. 2000; G. W. Henry et al. 2000), microlensing (e.g., OGLE 2005-BLG-390Lb; J. P. Beaulieu et al. 2006), and direct imaging (e.g., β Pic b; A. M. Lagrange et al. 2009), which are by far the most effective exoplanet detection methods. The ongoing study of exoplanets has contributed significant insights into the diversity and abundance of planetary systems within the Galaxy. As these systems vary greatly in physical and orbital characteristics, their study is of fundamental importance for the understanding of planet formation and evolution. Especially, the detection and characterization of hot ($P < 10$ days) and warm (10 days $< P <$ 300 days) Jupiter-mass planets provides an ideal testing ground for studying theories of planet formation (see e.g., R. I. Dawson & J. A. Johnson 2018; A. Emsenhuber et al. 2021a).

Hot and warm Jovian exoplanets have relatively short orbital periods, making them easy to detect with the RV and transit methods and to study their properties in detail. The orbits of hot Jupiters are subject to tidal interactions with their host stars, which result in a rapid circularization process and a loss of information regarding the formation history of the planets. Warm Jupiters, however, orbit their stars at greater distances and are much more likely to maintain their original orbital eccentricities (see R. I. Dawson & J. A. Johnson 2018 and references therein) and stellar obliquities (see S. H. Albrecht et al. 2022 and references therein), given the weaker tidal interactions. Therefore, the study of warm Jupiters offers a unique opportunity to understand the past interaction with the protoplanetary disk during the planetary formation and migration stage.

The aim of the Warm gIaNts with tEss (WINE) survey is the discovery and orbital and physical characterization of warm giants revealed by the Transiting Exoplanet Survey Satellite (TESS; G. R. Ricker et al. 2014), using precise Doppler follow-up observations. The WINE follow-up survey has been highly successful to date, having detected and characterized a significant number of warm giant planets (e.g., HD 1397 b; R. Brahm et al. 2019; TOI-150 b and TOI-163 b; D. Kossakowski et al. 2019; HD 213885 b; N. Espinoza et al. 2020; TOI-677 b; A. Jordn et al. 2020; TOI-481 b and TOI-892 b; R. Brahm et al. 2020; TOI-2179 b; M. Schlecker et al. 2020; TOI-216; R. I. Dawson et al. 2021; TOI-2202; T. Trifonov et al. 2021; TOI-201; M. J. Hobson et al. 2021; TOI-199; M. J. Hobson et al. 2023; TOI-2373, TOI-2416, and TOI-2524; J. Eberhardt et al. 2023; TIC 279401253; V. Bozhilov et al. 2023; TOI-2525; T. Trifonov et al. 2023; TOI-2529 and TIC 279401253; M. I. Jones et al. 2024; TOI-2328, TOI-3837, TOI-5027, and TOI-6628; M. Tala Pinto et al. 2025; TOI-4504; M. Vítková et al. 2025), including two warm Jupiters on highly eccentric orbits (TOI-2179b and TOI-6628b) and multiple systems consisting of pairs of warm giants near mean-motion resonance (MMR; TOI-2202, TIC 279401253, and TOI-2525), as well as a warm Jupiter with the strongest transit-timing-variations (TTVs) reported to date (TOI-4504).

In this work, we report the discovery and dynamical characterization of a system of two warm giants orbiting the late F dwarf star TOI-6695 as part of the WINE survey. TOI-6695 is very similar to the Sun, with $T_{\rm eff} = 6400$ K, [Fe/H] = 0.2 dex, $\log g = 4.2$ log cm s^{-2}, $M_* = 1.34\,M_\odot$, and $R_* = 1.52\,R_\odot$. Apart from its higher temperature, the stellar parameters are consistent with so-called Solar analogs, defined to satisfy 4.04 log cm s^{-2} $< \log g <$ 4.84 log cm s^{-2}, $-0.3 <$ [Fe/H] < 0.3, 5472 K $< T_{\rm eff} <$ 6072 K (C. Lehmann et al. 2022). The planets TOI-6695b and c orbit their host star on low-eccentricity orbits and are close to a 3:1 MMR. Therefore, the newly discovered TESS planets provide invaluable insights into both the history of their system and the theories of planetary formation and evolution.

In Section 2, we present the photometric and spectroscopic observational data obtained for TOI-6695 and which we use to characterize the orbital and physical parameters of the TOI-6695 pair of exoplanets. Section 3 describes the derivation of the stellar parameters from HARPS spectra and Gaia DR3 data. In Section 4, we introduce our data analysis and our global orbital analyses based on TESS photometry and our RV measurements. Our results are discussed in Section 5, and finally, we provide a summary and conclusions of our work in Section 6.

2. Observations

2.1. Photometric Data

2.1.1. TESS Photometry

TOI-6695 was first observed in sector 8 by TESS during its primary mission, and data are available with a cadence of 30 minutes. We identified the target as a candidate based on an analysis of the lightcurve generated by `tesseract`[28] from TESS full-frame images (FFIs), where we automatically search for individual transit-like features produced by giant planets (e.g., M. Schlecker et al. 2020). During the extended mission, TOI-6695 was observed in sectors 34, 35, and 61, and the data are available with a cadence of 2 minutes.

The 2 minute cadence light curves were provided by the Mikulski Archive for Space Telescopes (MAST).[29] We selected the data processed by the Science Processing Operations Center (SPOC; J. M. Jenkins et al. 2016). The SPOC data products include both simple aperture photometry (SAP) and systematics-corrected Pre-search Data Conditioning photometry (PDCSAP; M. C. Stumpe et al. 2012, 2014; J. C. Smith et al. 2012).

We examined the Target Pixel Files (TPFs), visualized with `tpfplotter` (A. Aller et al. 2020), to identify possible contamination from nearby sources. Figure 1 shows the four TPF frames of TOI-6695 for sectors 8, 34, 35, and 61. These images show the field surrounding the target, overplotted with an aperture grid that indicates the pixels that were used to determine the flux, as well as nearby Gaia DR2 sources. Within the aperture of TOI-6695, we found that the TIC 118339698 faint source contaminates the flux from TOI-6695. Therefore, for TESS sector 8, we determined the dilution factor according to N. Espinoza et al. (2019) as 0.98, which we used to correct the light curves for contribution. The dilution factor is defined as $D = \frac{1}{1+\sum_n F_n / F_T}$, with F_n being the flux of contaminating sources in the aperture and F_T being the out-of-transit flux of the target. The 2 minute PDCSAP cadence data for sectors 34, 35, and 61 from MAST had already been corrected for contamination from nearby stars and instrumental systematics. Thus, no dilution correction was applied for the flux time series collected in these sectors.

[28] https://github.com/astrofelipe/tesseract
[29] https://mast.stsci.edu/portal/Mashup/Clients/Mast/Portal.html

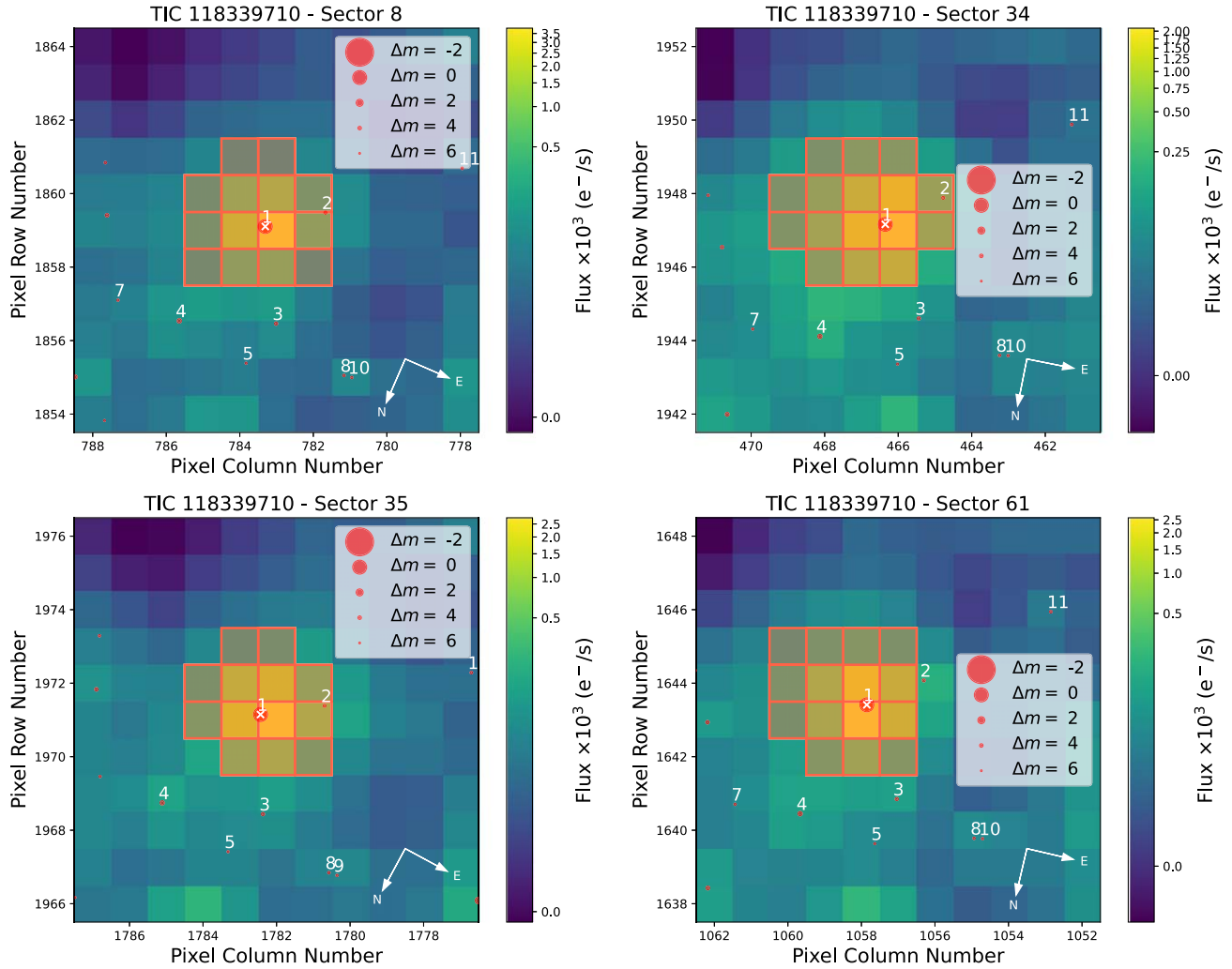

Figure 1. TESS TPFs of TOI-6695 (TIC 118339710), created using `tpfplotter`. Orange overlays show the aperture used to determine the flux (a white overlay indicates an automatically detected threshold aperture). Gaia DR2 catalog objects are shown as filled red circles sized according to their brightness relative to the target (marked with a white cross).

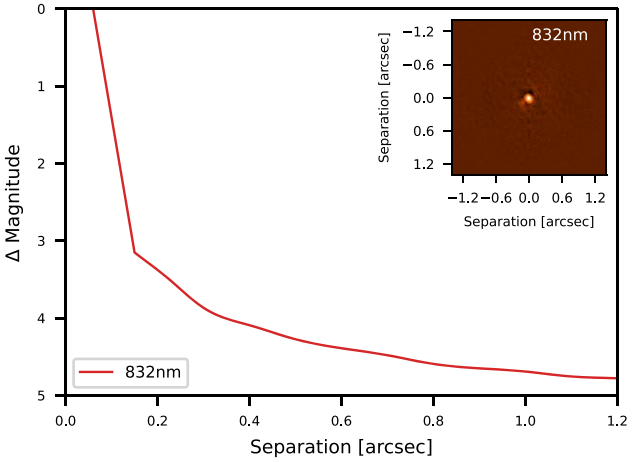

Figure 2. Speckle observations for TOI-6695 with NESSI. The red curve represents the 5σ contrast curve. The inset shows the reconstructed image of the star.

2.1.2. Ground-based Photometry at Observatoire Moana

The pixel scale of the TESS cameras is large (21″ pixel^{-1}), making photometric measurements often contaminated by nearby sources. To identify possible false positive scenarios, as well as to confirm the predicted timing of the transit, we used ground-based photometry from a robotic network of telescopes named Observatoire Moana. Specifically, we used two stations of the network installed at the El Sauce Observatory in Rio Hurtado, Chile. These stations are known as OMES-CDK600 and OMES-RiDK500. OMES-CDK600 is a 0.6 m CDK telescope coupled to an Andor iKon-L 936 deep depletion 2 k × 2 k CCD with a pixel scale of 0.″67 pixel^{-1}. OMES-RiDK500 is a 0.5 m Riccardi Dall–Kirkham telescope coupled to an Andor iKon-L 936 deep depletion 2k × 2k CCD with a pixel scale of 0.″79 pixel^{-1}. We used OMES-CDK600 and OMES-RiDK500 on the night of 2024 March 5 to monitor the same transit event of TOI-6695. We adopted an exposure time of 6 s and 12 s for OMES-CDK600 and OMES-RiDK500, respectively, and used an *r*' filter in both cases. OM-ES data is processed with an automated custom-made pipeline (J. I. Espinoza-Retamal et al. 2023; T. Trifonov et al. 2023).

2.1.3. Speckle Imaging

The NN-Explore Exoplanet Stellar Speckle Imager (NESSI; N. J. Scott et al. 2018) was used to observe TOI-6695 on 2022 April 18. We obtained a 1 minute sequence of diffraction-limited 40 ms exposures in the 832 nm filter on the red camera.

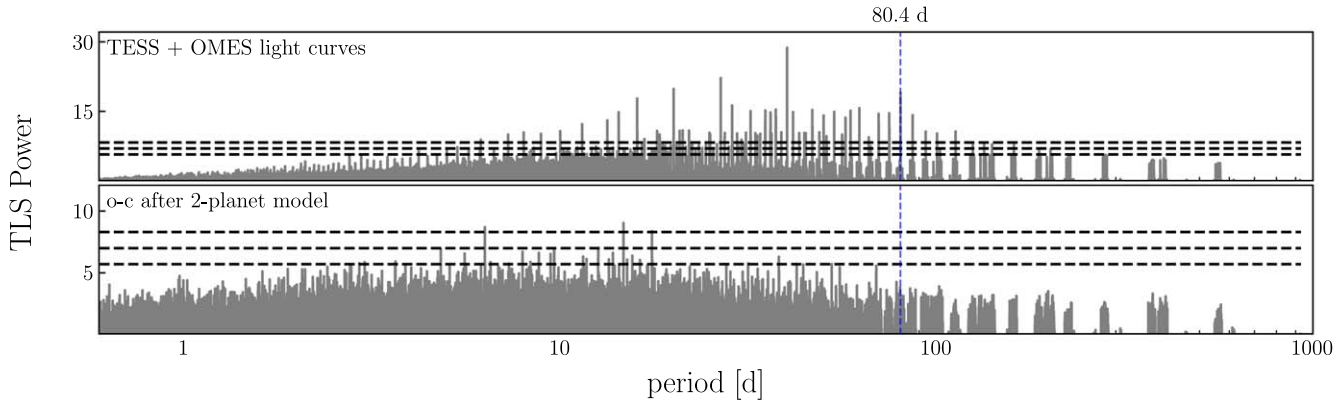

Figure 3. TLS power spectrum periodogram of TOI-6695. The top panel shows the results of the detrended and normalized TESS and OMES light curves. The bottom panel shows the residual TLS power after subtracting the full photodynamical model. The dashed blue line represents the orbital period of the transiting planet candidate, whereas dashed horizontal lines indicate the TLS signal detection efficiency (M. Hippke et al. 2019) power levels of 5.7, 7.0, and 8.3, which correspond to false-alarm-probability (FAP) levels of 10%, 1%, and 0.1%, respectively.

These exposures were processed following S. B. Howell et al. (2011) to produce a reconstructed image of the star, which we show in Figure 2 alongside the 5σ contrast limits for separations from 0.″2 to 1.″2. The NESSI data rule out the presence of blended companions or foreground or background sources down to a magnitude limit of $\Delta m_{832\mathrm{nm}} = 3.38$ at 0.″2 and $\Delta m_{832\mathrm{nm}} = 4.78$ at 1.″2.

2.2. Spectroscopic Data

TOI-6695 was observed with the spectroscopic instruments HARPS, CHIRON, PFS, CORALIE, FEROS, and TRES. In the following, we give details to the individual spectra for all instruments, except TRES, since they are only preliminary vetting data and don't contribute significantly to the analysis, so we didn't include them.

2.2.1. FEROS

The Fiber-fed Extended Range Optical Spectrograph (FEROS; A. Kaufer et al. 1999) is an echelle spectrograph mounted on the 2.2 m MPG/ESO[30] telescope at ESO's La Silla Observatory, Chile. FEROS is a highly efficient spectrograph with a resolving power of $R = 48{,}000$, covering the visible wavelength range from ∼350 nm to ∼920 nm. FEROS's achievable RV precision is approximately 10 m s^{-1}, which is sufficient for validating massive exoplanets detected by TESS in the southern celestial hemisphere. From 2020 March 1 to 2022 May 5, we obtained 16 FEROS spectra for TOI-6695. From these spectra we extracted the RV measurements and stellar activity indicators bisector span (BIS; e.g., D. Queloz et al. 2001a), H_α (I. Boisse et al. 2009), He I, log RHK (R. W. Noyes et al. 1984; D. K. Duncan et al. 1991), and Na II (J. Gomes da Silva et al. 2011), using the Collection of Elemental Routines for Echelle Spectra pipeline (CERES; R. Brahm et al. 2017a). The FEROS RVs and stellar activity measurements for our target are listed in Table A2. The RVs have a mean error of 11.3 m s^{-1}, and an rms of 40.3 m s^{-1}. Due to the high RV scatter and 5 out of the 16 RVs being outliers, we chose not to use the FEROS data for our analysis.

[30] MPG = Max-Planck-Gesellschaft = Max Planck Society; ESO = European Southern Observatory.

Table 1
Stellar Parameters of TOI-6695

Parameter	Value	Reference
Names	TIC 118339710, TOI-6695	TIC v8.2
	5701679002245319296	Gaia DR3
R.A. (J2000)	08^h 38^m 17.″2895456952	Gaia DR3
decl. (J2000)	−23° 33′ 00.″826834104	Gaia DR3
distance [pc]	282.670 ± 0.967	Gaia DR3
T [mag]	10.354	TIC v8.2
B [mag]	11.351	TIC v8.2
V [mag]	10.768	TIC v8.2
J [mag]	9.816	TIC v8.2
H [mag]	9.599	TIC v8.2
K [mag]	9.512	TIC v8.2
Spectral type	F5V - G0V	P&M
T_{eff} [K]	6400 ± 100	this work
$\log g$ [log cm s^{-2}]	4.202 ± 0.015	this work
$R_\star$ [$R_\odot$]	$1.517^{+0.023}_{-0.022}$	this work
$M_\star$ [$M_\odot$]	$1.338^{+0.023}_{-0.022}$	this work
$L_\star$ [$L_\odot$]	3.47 ± 0.18	this work
$\rho_\star$ [kg m^{-3}]	540^{+26}_{-25}	this work
[Fe/H] [dex]	0.2 ± 0.05	this work
$v \cdot \sin i$ [km s^{-1}]	6.7 ± 0.3	this work
Age [Gyr]	2.1 ± 0.3	this work
A_V [mag]	0.28 ± 0.07	this work

Note. P&M: M. J. Pecaut & E. E. Mamajek (2013) TIC v8.2: K. G. Stassun et al. (2019), M. Paegert et al. (2021) Gaia DR3: Gaia Collaboration (2020), Gaia Collaboration et al. (2023).

2.2.2. HARPS

We performed observations of TOI-6695 with the HARPS spectrograph (M. Mayor et al. 2003) installed at the 3.6 m telescope at La Silla. We obtained 53 spectra between 2020 March 18, and 2024 March 15 and processed the spectra using the CERES pipeline (R. Brahm et al. 2017a), providing both RVs as well as BIS, Hα, Ca II, Na II, and He I (J. Gomes da Silva et al. 2011) activity indicators. The HARPS measurements are listed in Table A3. The RVs have a mean error of 4.0 m s^{-1}, and an rms of 46.3 m s^{-1}.

2.2.3. CHIRON

TOI-6695 was observed with the CHIRON spectrograph (A. Tokovinin et al. 2013) at the Small and Moderate Aperture

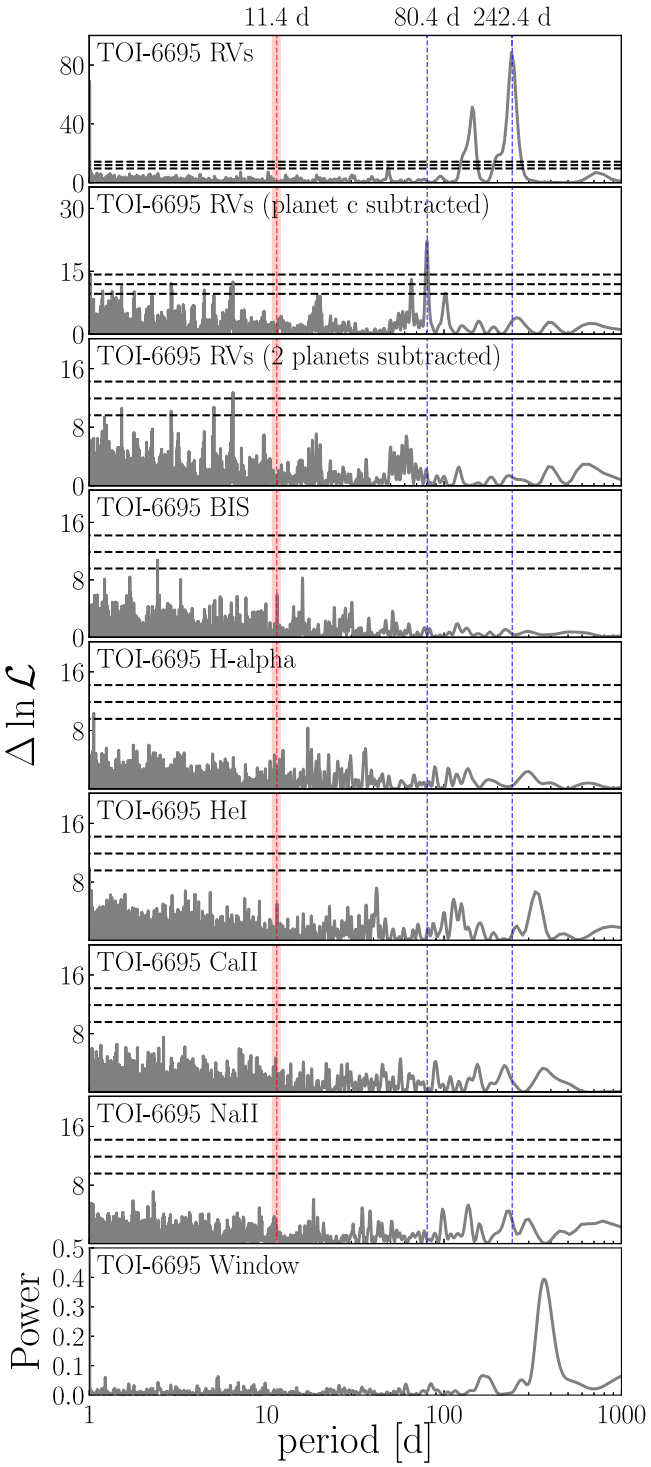

Figure 4. MLP periodograms for RV and stellar activity data of TOI-6695. The top four panels show the periodograms of the raw and residual RVs after subtracting Keplerian models, panels 5–9 show the periodograms of the stellar activity indicators and the bottom panel shows the RV window function. Dashed blue lines indicate the planetary orbital periods, and the red dashed line and shaded region correspond to the assumed stellar rotational period. Dashed horizontal lines correspond to FAP levels of 10%, 1%, and 0.1%.

Research Telescope System (J. P. Subasavage et al. 2010) 1.5 m telescope at CTIO. We obtained a total of 33 spectra between 2020 December 1, and 2023 May 4. We used the slit mode ($R \sim 80{,}000$) with an exposure time between 1200 and 1800 s, leading to a typical signal-to-noise ratio (SNR) per pixel of ~25–35, and ~10–20 m s^{-1} 1σ RV uncertainties at a wavelength of ~550 nm (A. Tokovinin et al. 2013). The data were automatically processed and reduced by the Yale pipeline (L. A. Paredes et al. 2021), and the RVs were obtained using the pipeline described in M. I. Jones et al. (2019). The RVs have a mean error of 14.6 m s^{-1}, and an rms of 26.2 m s^{-1}.

2.2.4. CORALIE

TOI-6695 was observed with the CORALIE spectrograph (D. Queloz et al. 2001b) at the Swiss 1.2 m Euler telescope at La Silla by both the WINE and Swiss teams. In total, 18 spectra were obtained between 2020 January 20, and 2022 May 27, with a median exposure duration of 1200 s. CORALIE is a fiber-fed echelle spectrograph with a 2″ science fiber and a secondary fiber with a Fabry–Perot for simultaneous wavelength calibration. It has a spectral resolution of $R = 60{,}000$. RVs are extracted using the standard CORALIE DRS by cross-correlating the spectra with a binary G2V template (A. Baranne et al. 1996; F. Pepe et al. 2002). The BIS, FWHM, and other line-profile diagnostics were also computed via the CORALIE DRS, as was the H_α index for each spectrum to check for possible variation in stellar activity. The resulting RVs and activity indicators are listed in Table A5. The RVs have a mean error of 20.0 m s^{-1}, and an rms of 27.4 m s^{-1}.

2.2.5. PFS

We observed TOI-6695 with the Planet Finder Spectrograph (PFS; J. D. Crane et al. 2006, 2008, 2010), which is mounted on the 6.5 m Magellan II (Clay) Telescope at Las Campanas Observatory in Chile. PFS is a slit-fed echelle spectrograph with a wavelength coverage of 391–734 nm. Wavelength calibration is achieved via an iodine gas cell, which also allows characterization of the instrumental profile. We used a 0.″3 slit and obtained 16 spectra on 11 epochs, observed through iodine, between 2020 December 22, and 2022 January 23, with exposure times of 900 or 1200 s. Any contiguous spectra were binned together into a single epoch. We also obtained a high-SNR, iodine-free template observation. The radial velocities were extracted using a custom IDL pipeline that flat fields, removes cosmic rays, and subtracts scattered light, following the prescriptions of G. W. Marcy & R. P. Butler (1992) and R. P. Butler & G. W. Marcy (1996). The mean internal precision achieved is 2.49 m s^{-1} and the rms is 17.6 m s^{-1}. The radial velocities are presented in Table A6.

3. Stellar Parameters

We followed the procedure initially presented in R. Brahm et al. (2019) to determine the stellar atmospheric and physical parameters. This is a two-step iterative process. The first step consists of the comparison of the observed co-added HARPS spectra to a library of synthetic spectra (F. Castelli & R. L. Kurucz 2004) using the `zaspe` code (R. Brahm et al. 2017b). This procedure allows us to estimate the atmospheric parameters of the star ($T_{\rm eff}$, $\log g$, [Fe/H], and $v \sin i$). The second step involves a spectral energy distribution (SED) fit to public available broad-band magnitudes of the star. The model in this case corresponds to synthetic magnitudes of the PARSEC stellar evolutionary models transformed to apparent magnitudes using theGaia DR3 parallax (Gaia Collaboration et al. 2018). In this step we fix the metallicity of the models to the value obtained with `zaspe` and we use the $T_{\rm eff}$ obtained with `zaspe` as a prior. This procedure allows us to estimate the

Table 2
Nested-sampling Priors, Posteriors, and the Optimum $-\ln \mathcal{L}$ Orbital Parameters of the Two-planet System Derived by Joint *N*-body Modeling of TESS and Moana Transit Photometry and RV Data Taken with CORALIE, HARPS, PFS, and CHIRON

	Median and 1σ		Max. $-\ln \mathcal{L}$		Adopted Priors	
Parameter	Planet b	Planet c	Planet b	Planet c	Planet b	Planet c
K [m s^{-1}]	$8.0^{+0.6}_{-0.6}$	$39.0^{+0.7}_{-0.6}$	7.9	39.0	$\mathcal{U}(5, 30)$	$\mathcal{U}(35, 45)$
P [days]	$80.389^{+0.003}_{-0.005}$	$242.4^{+0.4}_{-0.3}$	80.385	242.7	$\mathcal{U}(80.22, 80.96)$	$\mathcal{U}(239, 249)$
$e \sin(\omega)$	$0.028^{+0.007}_{-0.005}$	$-0.016^{+0.004}_{-0.004}$	0.037	−0.014	$\mathcal{U}(-0.1, 0.1)$	$\mathcal{U}(-0.1, 0.1)$
$e \cos(\omega)$	$-0.030^{+0.007}_{-0.019}$	$-0.01^{+0.01}_{-0.02}$	−0.025	−0.01	$\mathcal{U}(-0.1, 0.1)$	$\mathcal{U}(-0.1, 0.1)$
λ [deg]	$86.2^{+0.8}_{-2.2}$	139^{+2}_{-2}	86.8	141	$\mathcal{U}(45, 135)$	$\mathcal{U}(0, 360)$
i [deg]	$90.62^{+0.02}_{-0.02}$	90	90.64	90	$\mathcal{U}(89, 91)$	(fixed)
e	$0.040^{+0.006}_{-0.007}$	$0.022^{+0.006}_{-0.007}$	0.044	0.015	(derived)	(derived)
ω [deg]	137^{+26}_{-12}	-121^{+22}_{-69}	124	−111	(derived)	(derived)
M_0 [deg]	307^{+12}_{-26}	261^{+72}_{-23}	323	252	(derived)	(derived)
m_p [$M_{\rm Jup.}$]	$0.21^{+0.01}_{-0.01}$	$1.45^{+0.03}_{-0.03}$	0.20	1.45	(derived)	(derived)
r_p [$R_{\rm Jup.}$]	$0.85^{+0.02}_{-0.02}$	…	0.75	…	(derived)	…
ρ_p [g cm^{-3}]	$0.41^{+0.04}_{-0.04}$	…	0.60	…	(derived)	…
a_p [au]	$0.402^{+0.002}_{-0.002}$	$0.838^{+0.005}_{-0.005}$	0.402	0.839	(derived)	(derived)
$T_{\rm eq.}$ [K]	599^{+8}_{-8}	415^{+6}_{-5}	599	415	(derived)	(derived)

Note. The adopted priors, listed in the right-most columns, are uniform (flat) priors, assigning equal probability to all values within the allowed ranges. The orbital elements are in the Jacobi frame and are valid for epoch BJD = 2458400.0. The derived planetary posterior parameters of a, and m are calculated taking into account the stellar parameter uncertainties. The value listed for the mass m_p of planet c is the minimum dynamical mass m. We fixed $\Delta\Omega = 0$; thus, the mutual inclination in the model comes from the difference between $i_b - i_c$.

age of the star, along with its mass and radius, which can be used to obtain a more precise value for the $\log g$ than the one reported by `zaspe`. In the next iteration with `zaspe` we fix the $\log g$ value to the one obtained with the SED fit. The iterations end when reaching convergence in $T_{\rm eff}$ and [Fe/H] of two consecutive `zaspe` runs.

We find that TOI-6695 is a late-F-type star ($T_{\rm eff} = 6400 \pm 100$ K) in the main sequence with a mass of $1.34 \pm 0.02\ M_\odot$ and a radius of $1.52 \pm 0.02\ R_\odot$. It is metal-rich ([Fe/H] $= 0.20 \pm 0.05$) and has a projected rotational velocity of $v \sin i = 6.7 \pm 0.3$ km s^{-1}. The stellar parameters and observational properties of TOI-6695 are presented in Table 1.

4. Analysis and Results

4.1. Period Search Analysis in TESS

We detrended the 30 minutes FFI cadence TESS lightcurve for sector 8 as well as the preprocessed 2 minute cadence light curves provided by MAST by using the `wotan` package (M. Hippke et al. 2019). For this purpose, we apply a Gaussian Process model with a Matern 3/2 kernel of size 5 days.

After detrending the 30 minutes cadence lightcurve, we performed a period search on all light curves using the `transitleastsquares` package (TLS; M. Hippke & R. Heller 2019). The top panel of Figure 3 shows the TLS power of the TESS and OMES light curves of TOI-6695, and the bottom panel shows the TLS results of the residual light curves after subtracting the two-planet *N*-body model. The top panel shows many significant signals, most prominent at $P = 40.2$ days, which we could determine to be the harmonics and subharmonics of the orbital period of the planetary candidate $P_b = 80.4$ days, which is shown as a dashed blue line. The bottom panel shows that subtracting a model for both planets removes the signal and leaves the residual periodogram with no additional significant signals.

4.2. Period Search Analysis in RV Data

Following the initial transit candidate discovery, we observed TOI-6695 with various spectroscopic instruments to confirm the planetary nature of the transit signals, as well as to disentangle the correct orbital period of the transiting planet. Figure 4 shows the Maximum Likelihood Periodograms (MLPs; R. V. Baluev 2009; M. Zechmeister et al. 2019) for the RV data. The top three panels show the likelihood of the combined HARPS, CHIRON, PFS, and CORALIE RVs after subtracting a model with only planet c, after subtracting a model with only planet b, and the residual periodogram after subtracting the combined two-planet model. The following five panels show the periodograms of the BIS, Hα, HeI, $\log R^{'}_{\rm HK}$, and Na II activity indicators obtained from the HARPS RVs; the bottom panel shows the window function of the combined RVs. Analogous to Figure 3, dashed blue lines represent the orbital periods of the planetary candidates, and the red dashed line corresponds to the assumed rotational period of TOI-6695. We determined the maximum possible rotational period of TOI-6695 as $P_{\rm rot}/\sin i = 2\pi R_\star / v \sin i$ by using the stellar radius and projected rotational velocity from Table 1. A periodogram inspection of the TESS light curves did not provide any evidence for rotational modulation. Assuming an orbital alignment of the stellar spin to the orbit of TOI-6695b, we found a rotational period of $P_{\rm rot} = 11.4^{+0.5}_{-0.6}$ days, which is indicated as a red dashed line and shaded region in Figure 4. In the base RV periodogram, instead of the 40.2 days signal, a new 241.3 days signal can be seen, which is not present in the TLS analysis. After subtracting a Keplerian model with the same period, the residual periodogram showed a significant signal at $P = 80.4$ days. A combined two-planet Keplerian model with both signals left no significant signals in the residuals. Neither signal has a counterpart in the stellar activity periodogram, and neither signal coincides with the stellar rotational period. Due to the unfavorable situation that the three

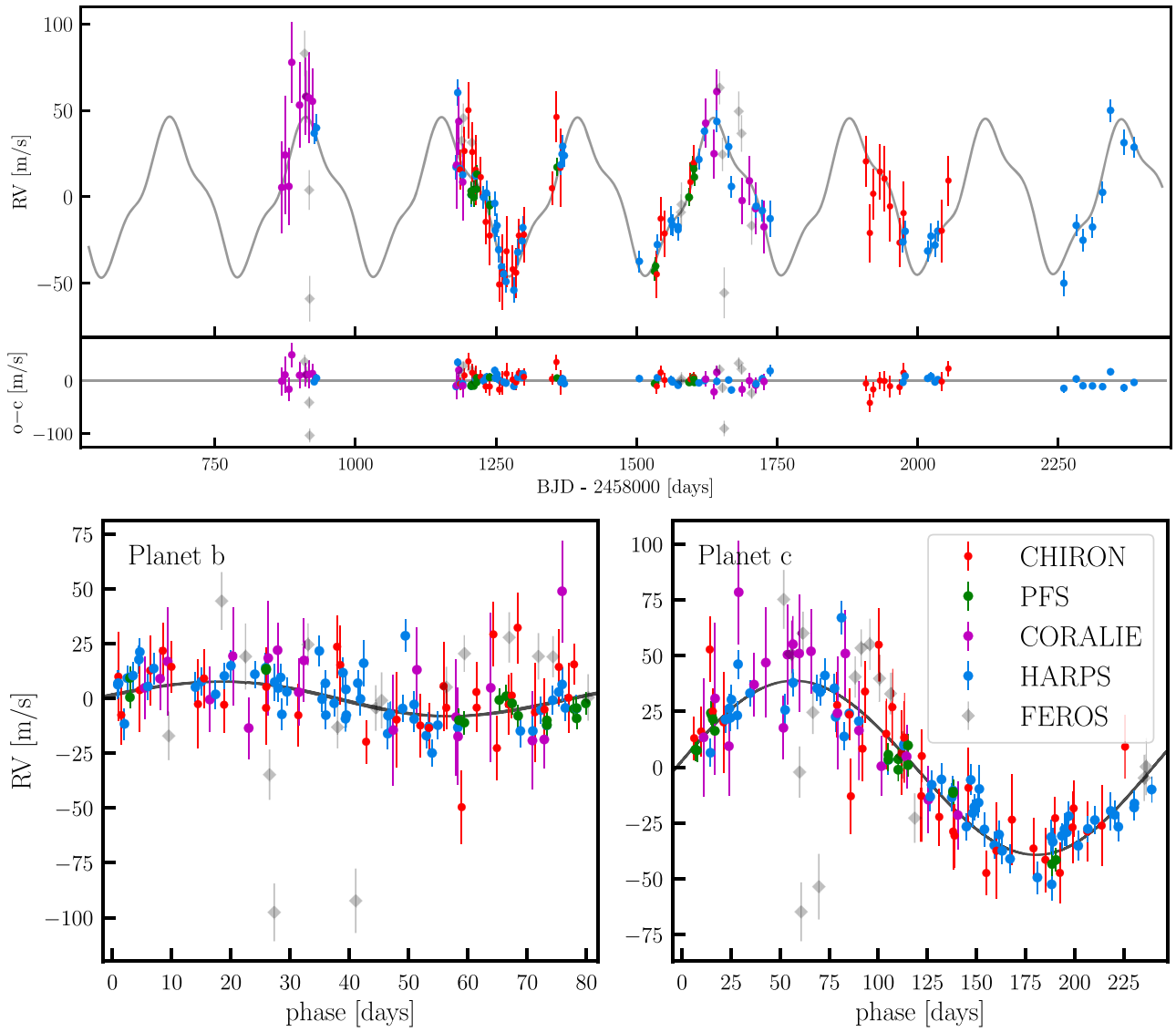

Figure 5. Radial velocity time series (top panel) and phase-folded plots of the planetary signals (TOI-6695b, bottom left; TOI-6695c, bottom right). In addition to the RVs from HARPS, CHIRON, PFS, and CORALIE, FEROS data are overlayed as grayed-out diamonds, to show their general agreement with our model, but also their overall poor quality.

transits that were observed by TESS are equally spaced, as well as the close proximity to the 3:1 mean-motion resonance commensurability, it required several models and the observation of our predicted transit on 2024 March 5 (see Section 2.1.2) to be convinced of the periods for our model.

4.3. Joint Transit and RV Orbital Fitting

We performed a combined RV and transit photometry orbital analysis of TOI-6695 by using an *N*-body model included in the `Exo-Striker`[31] (T. Trifonov 2019) exoplanet toolbox. The `Exo-Striker` employs the `batman` package (L. Kreidberg 2015) for transit lightcurve models, and the RV model formalism in M. H. Lee & S. J. Peale (2003). For the posterior analysis, the `Exo-Striker` utilizes the nested-sampling (NS) algorithm in combination with the `dynesty` package (J. S. Speagle 2020). The NS configuration in this work is similar to the one used in T. Trifonov et al. (2021). We used 100 "live-points" per fitted parameter with a "dynamic" NS sampler approach (see J. S. Speagle 2020 for details). The priors for the parameters were determined through a series of consecutive NS runs, starting with initial values derived from the TLS and MLP signal vetting analyses. We simultaneously modeled the *N*-body osculating orbital parameters for the TOI-6695 system, and the nuisance RV data parameters and transit lightcurve parameters, deriving posteriors from the NS results.

The parameters we fitted for each planet in the model were the RV semiamplitude K, the orbital period P, and mean longitude λ valid for BJD = 2458525.6 (slightly before the first TESS midtransit event). Instead of the eccentricity e and longitude of periastron ω we chose to use the $e \sin \omega$, $e \cos \omega$ parameterization. The transit model parameters are shared with these from the RV model but also include the orbital inclination i, time of midtransit t_0, and the relative to the stellar radius semimajor axis $a/R_\star$ and planetary radius $r/R_\star$. Transit model parameters are quadratic limb-darkening coefficients u_1 and u_2 separately for TESS and Moana. Additionally, we fit the transit and RV data offsets and jitter parameters $\mathrm{RV}_{\mathrm{offset}}$, $\mathrm{RV}_{\mathrm{jitter}}$,

[31] https://github.com/3fon3fonov/exostriker

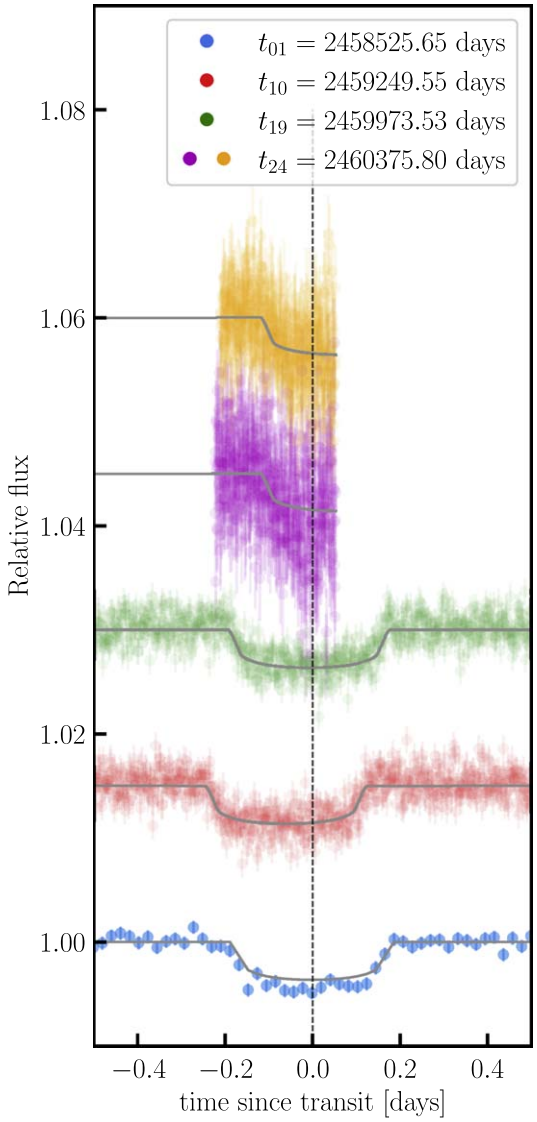

Figure 6. Individual transits for TOI-6695. `blue`:TESS sector 8; `red`:TESS sector 34; `green`:TESS sector 61; `purple/orange`: ground-based data from OM-ES.

$\text{transit}_{\text{offset}}$ and $\text{transit}_{\text{jitter}}$ for the different instruments. From the posterior probability distribution, we derived posteriors for the orbital eccentricity e, the argument of periastron ω, mean anomaly MA, planetary mass m_p (or minimum dynamical mass m_p for TOI-6695c), semimajor axis (a_p), radius (r_p), mean density (ρ_p), and equilibrium temperature (T_{eq}) for both planets. Since no transits were detected in the light curves for TOI-6695c, we only modeled the transit parameters (t_0, $a/R_\star$, $r/R_\star$, r_p, and ρ_p) for the transiting planet, TOI-6695b. An estimate of transit times for TOI-6695c based on RV data, finds the planet transiting either during the TESS window or between TESS observations.

The results from our NS posteriors revealed that TOI-6695b is a warm Saturn with a mass of $m_b = 0.21^{+0.01}_{-0.01}\ M_{\text{jup}}$, a radius of $r_b = 0.85^{+0.02}_{-0.02}\ R_{\text{jup}}$, an orbital eccentricity of $e_b = 0.040^{+0.006}_{-0.007}$ and a bulk density of $\rho_b = 0.41^{+0.04}_{-0.04}$ g cm^{-3}. It orbits the host star at a distance of $a_b = 0.402$ au, corresponding to an orbital period of $P_b = 80.389$ days and an equilibrium temperature of $T_{\text{eq}} = 599^{+8}_{-8}$ K. TOI-6695c is a warm Jupiter with a minimum dynamical mass of $m_c = 1.45^{+0.03}_{-0.03}\ M_{\text{jup}}$ and an orbital eccentricity of $e_c = 0.022^{+0.006}_{-0.007}$. The distance to its host star is $a_c = 0.838$ au, corresponding to an orbital period of 242.4 days and an equilibrium temperature of $T_{\text{eq}} = 415^{+6}_{-5}$ K. In our model, we fixed the inclination of TOI-6695c to 90° and $\Delta\Omega$ to 0°, so the mutual inclination comes only from the difference $\Delta i = i_b - i_c$. Our NS result estimates are listed in Table 2 for the relevant orbital and derived parameters, as well as in Table A1 for the fitted nuisance parameters: the radial velocity offsets, transit offsets, and jitters, alongside the quadratic limb-darkening coefficients.

Figure 5 shows the available RV data alongside the RV part of our *N*-body model. The top panel shows the full RV time series, whereas the bottom panels show the phase-folded RVs for TOI-6695b, and c, respectively. HARPS data is shown as blue points, CHIRON as red, PFS as green, and CORALIE as purple. Due to the many outliers and large overall scatter, we did not include the FEROS data for our analysis and chose to only include them as grayed-out diamonds for completeness and to show that they are generally consistent with our model.

Figure 6 shows the photometric part of our joint *N*-body model with the individual transit events shown phase-folded with a period of 80.438 days, corresponding to a transit duration of 10.81 hr, derived from a fit to the data with a static period. The blue data represent sector 8 of the TESS light curves, the red data corresponds to sector 34, and the green data to sector 61. Purple and orange data show the ingress observed at the El Sauce Observatory of the Observatoire Moana network in two separate bands. The individual transits are offset and are shown relative to the midtransit time of the first detected transit, marked as a dashed line, showing TTVs caused by the outer planet. Our photodynamical model already incorporates the TTVs and the individual transit times are shown in the figure. The transit in sector 8 (blue data) shows a slightly anomalous depth. We inspected the lightcurve generated by `tesseract`, as well as the lightcurve generated by the TESS Quick Look Pipeline (QLP; M. Kunimoto et al. 2021) and the TESS-Gaia-Light-Curve pipeline (TGLC; T. Han & T. D. Brandt 2023). Figure A1 shows a comparison between tesseract, QLP and TGLC pipelines. The transit depth was largely consistent in all data reductions. The RV fit does not support this transit event being a caused by another planet, thus we attribute it to unexplained systematics.

4.4. Dynamical Modeling

Both planets TOI-6695b, and c, orbit their host star on low-eccentricity orbits. We studied the overall dynamics of the planetary system by using a numerical scheme similar to the one used for TOI-2202 (T. Trifonov et al. 2021) and TOI-2525 (T. Trifonov et al. 2023). From the full set of samples, we randomly chose 1000 and integrated them for 10 Myr using the Wisdom–Holman *N*-body integrator (also known as MVS; J. Wisdom & M. Holman 1991), which is implemented within the `Exo-Striker` toolbox. We adopted a numerical time step of 1 day, sufficiently sampling orbital timescales in the system. An integration time of 10 Myr corresponds to ∼45 million orbits of TOI-6695b, allowing us to derive robust conclusions about the system's stability and dynamics.

We monitored both the planetary semimajor axes and their orbital eccentricities evolve over the integrated time and rejected orbital configurations as unstable if either a_b or a_c deviated more than 10% of their initial value or if e_b or e_c

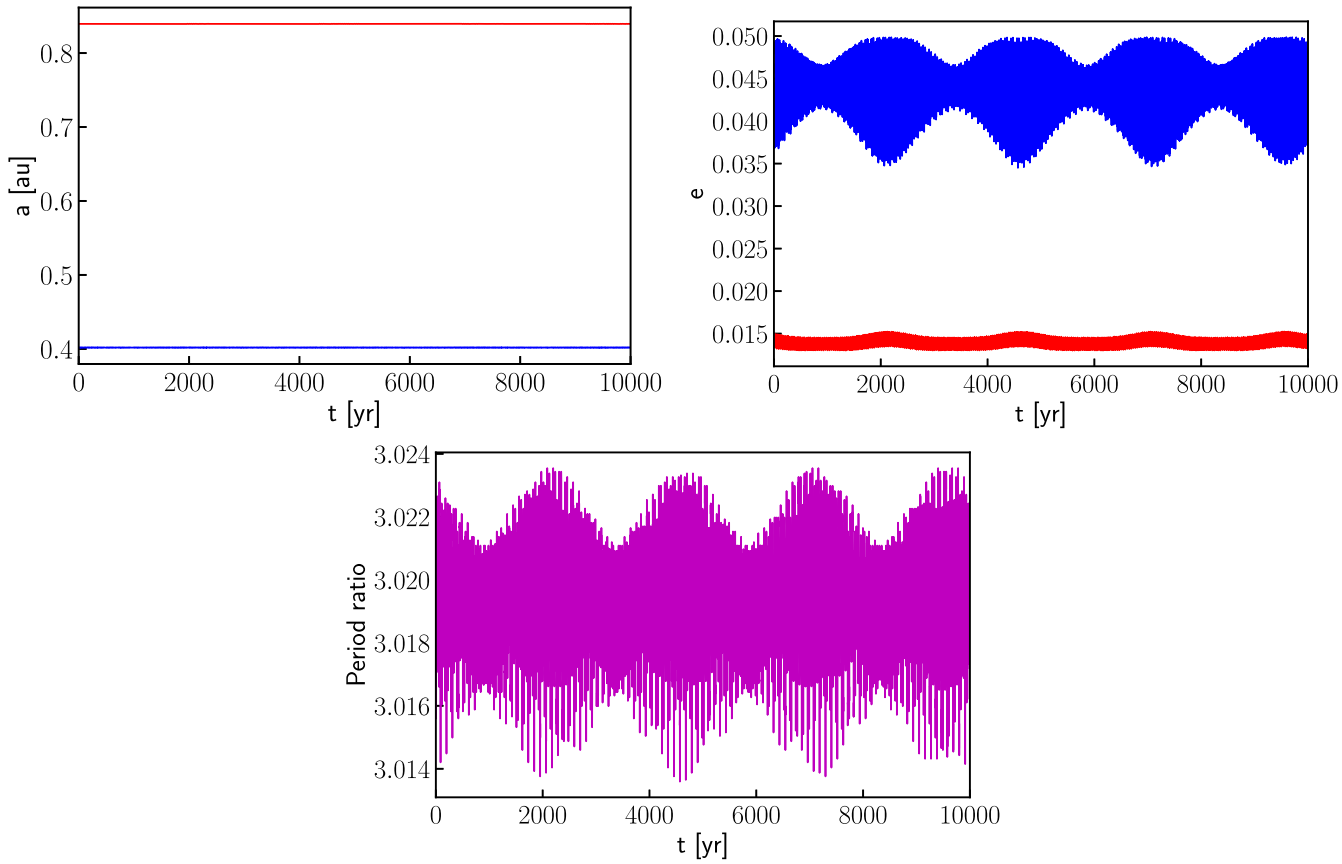

Figure 7. The top-left figure shows the orbital evolution of the planetary semimajor axes from the best fit. The top-right plot shows the evolution of the orbital eccentricities, `blue`: TOI-6695b; `red`: TOI-6695c. The bottom panel shows the evolution of the period ratio between the two massive planets.

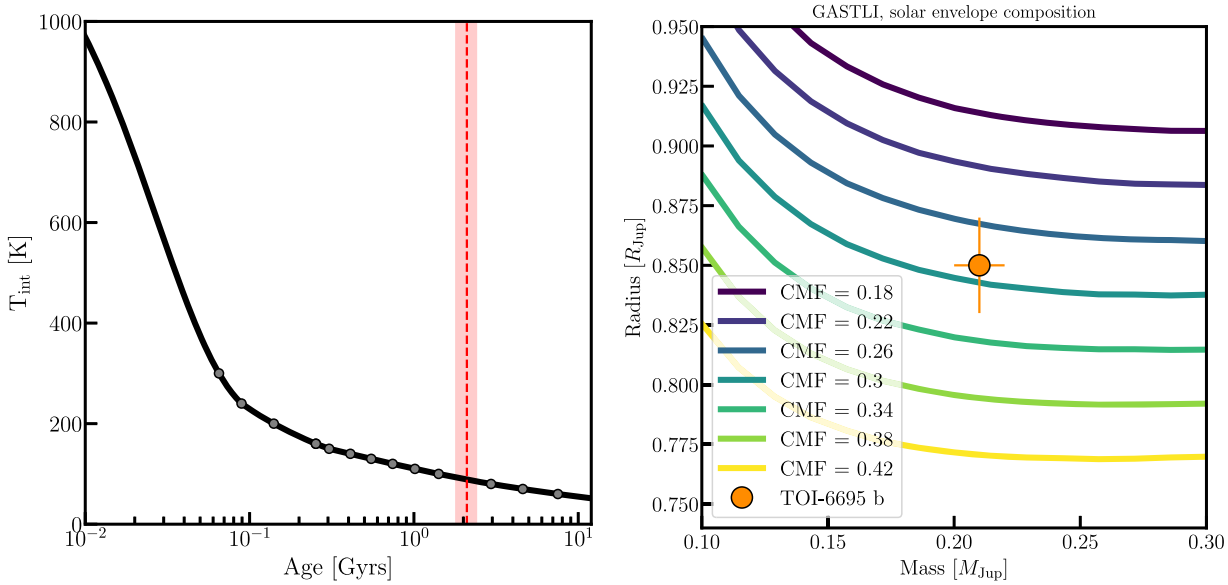

Figure 8. Thermal evolution for TOI-6695b of the internal temperature and mass–radius diagrams for varying core-mass-fractions, generated using GASTLI. We assumed a core-mass fraction CMF = 0.30 and a solar envelope composition to compute the thermal evolution of TOI-6695b. TOI-6695b's age of 2.1 ± 0.3 Gyr (shown as red dashed line and shaded region) is consistent with an internal temperature $T_{\rm int}$ = 50–150 K. Thus, we adopted a value of 100 K for our mass–radius relations. Given its mass, radius and age, TOI-6695b could present a CMF = 0.25–0.35 with a solar composition (see text).

became too large and led to crossing orbits. Figure 7 shows excerpts of 10,000 yr of evolution for the semimajor axes (left) and orbital eccentricities (right) of our best fit configuration. We find all samples to be long-term stable for 10 Myr in both semimajor axes and eccentricities. With a period ratio of ∼3.02, we examined the characteristic resonance angles of the 3:1 mean-motion resonance configuration

$$\theta_1 = \lambda_b - 3\lambda_c - 2\varpi_c \quad (1)$$

$$\theta_2 = \lambda_b - 3\lambda_c + \varpi_b - \varpi_c \quad (2)$$

$$\theta_3 = \lambda_b - 3\lambda_c + 2\varpi_b, \quad (3)$$

with the planetary longitudes of periastron $\varpi_{b,c} = \Omega_{b,c} + \omega_{b,c}$ and the mean longitides $\lambda_{b,c} = M_{0b,c} + \varpi_{b,c}$, as well as the secular apsidal angle $\Delta\omega$, which is defined as:

$$\Delta\omega = \omega_c - \omega_b, \quad (4)$$

and indicates whether the system is dominated by secular interactions if this angle librates around a fixed angle. We found all resonance angles circulating between 0° and 360°, indicating that the system is not in an actual MMR configuration.

4.5. Interior Modeling

We used the GAS gianT modeL for Interiors (GASTLI; L. Acuña et al. 2021, 2024)[32] to investigate the interior composition of TOI-6695b. GASTLI is a Python package specifically developed to model the internal structure volatile-rich exoplanets. It generates mass–radius and thermal evolution relationships (radius-age diagrams). In our analysis, the planetary interior is divided in two distinct layers: a core and an envelope. The core is assumed to contain a 1:1 mass ratio of rocks and water, while the envelope is composed of hydrogen, helium (H/He), and water, with water serving as a proxy for metals.

Our first step is to calculate a thermal evolution curve to estimate the internal (or intrinsic) temperature, $T_{\rm int}$, based on the age of TOI-6695b. The left panel of Figure 8 shows an age-$T_{\rm int}$ diagram, from which we constrained the internal temperature $T_{\rm int} = 50$–150 K, according to an age of 2.1 Gyr. Thus, we adopted a representative value of $T_{\rm int} = 100$ K to generate a mass–radius diagram (Figure 8, right panel). This diagram explores how the planet's radius varies with different core-mass fractions (CMF), assuming a fixed solar composition for the envelope.

From our analysis, we determined that TOI-6695b has a bulk metal-mass fraction of approximately 0.30, meaning that 30% of its total mass is composed of heavy elements. This is notably higher than Saturn's estimated bulk metal-mass fraction of about 0.20, despite TOI-6695b being slightly less massive. The higher metal content of TOI-6695b aligns with the predictions of the core accretion model of planet formation, which suggests a positive correlation between planetary mass and bulk metallicity. Additionally, this result is consistent with observed trends for both solar system giants and other exoplanets (D. P. Thorngren et al. 2016).

5. Discussion

Figures 9–11 put the planets discussed in this work in the broader context of all known transiting exoplanets orbiting stars with similar characteristics, including the solar system giant planets. The exoplanet properties displayed in these figures were selected from the TEPCAT catalog (J. Southworth 2011), based on the properties of their host stars: $-0.3 < [\mathrm{Fe/H}] < 0.3$; $4.04\ \mathrm{cm\ s^{-2}} < \log g < 4.84\ \mathrm{cm\ s^{-2}}$; $5472\ \mathrm{K} < T_{\rm eff} < 6500\ \mathrm{K}$.

Figure 9 shows the planetary masses (projected mass $m \sin i$ for TOI-6695c) plotted against the orbital separation, with the planets discussed in this work shown as big stars. As evident, TOI-6695b and c are located in the sparsely populated long-period region of warm giant demographics. Analogously,

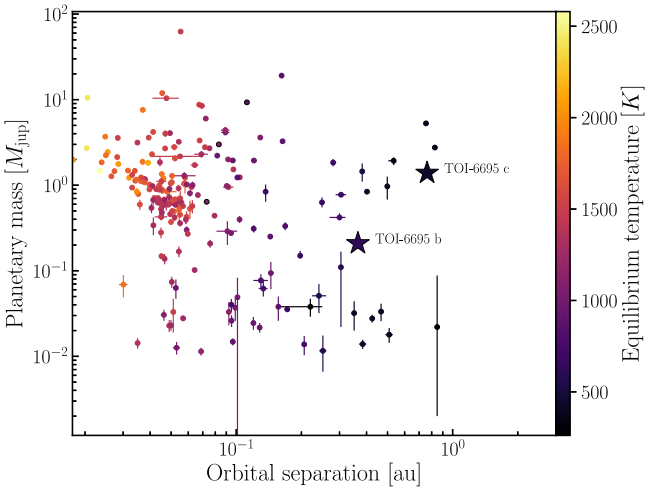

Figure 9. Mass-separation diagram for planets around Sun-like stars (definition according to C. Lehmann et al. 2022; see Section 1, modified to include TOI-6695b). The position of TOI-6695b and TOI-6695c are shown as star symbols.

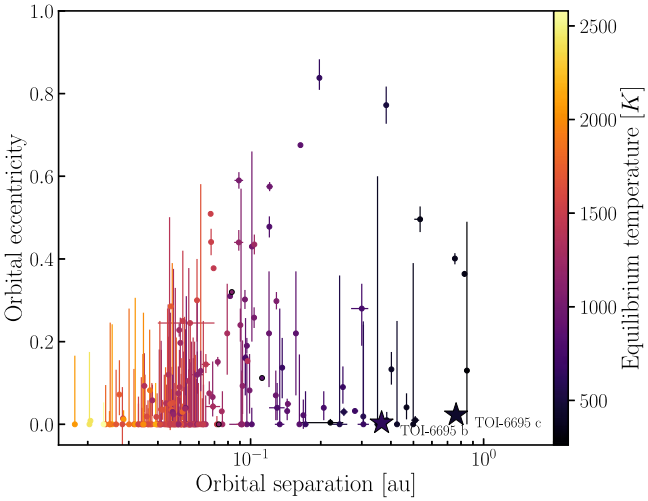

Figure 10. Same as of Figure 9, but for eccentricity against separation.

Figure 10 shows the same planets in an eccentricity-separation diagram, with the low-eccentricity planets TOI-6695b, and c shown as big stars. Figure 11 shows a mass–radius diagram that contains the solar system giant planets as blue stars in addition to TOI-6695b. This allows us to study the bulk densities for the planets, showing composition models based on C. Mordasini et al. (2012), L. Zeng et al. (2019), and A. Emsenhuber et al. (2021b) as solid lines of varying colors. TOI-6695b is consistent with the predictions by the displayed exoplanet composition models. With a projected rotational velocity of $v \cdot \sin i = 6.7\ \mathrm{km\ s^{-1}}$, the transiting planet TOI-6695b becomes an interesting target to measure the Rossiter–McLaughlin effect R. A. Rossiter (1924) and D. B. McLaughlin (1924). The estimated amplitude of the signal is $17.5\ \mathrm{m\ s^{-1}}$, which can be measured by high-resolution instruments.

TOI-6695b and c have a period ratio of 3.02, which is very close to a 3:1 mean-motion resonance configuration. This is a rare configuration with only 34 known examples,[33] such as 55 Cnc b & c (J. Ji et al. 2003; L.-Y. Zhou et al. 2004) and

[32] https://github.com/lorenaacuna/GASTLI

[33] https://exoplanetarchive.ipac.caltech.edu/; chosen to satisfy $2.95 < P_{\rm rat} < 3.05$.

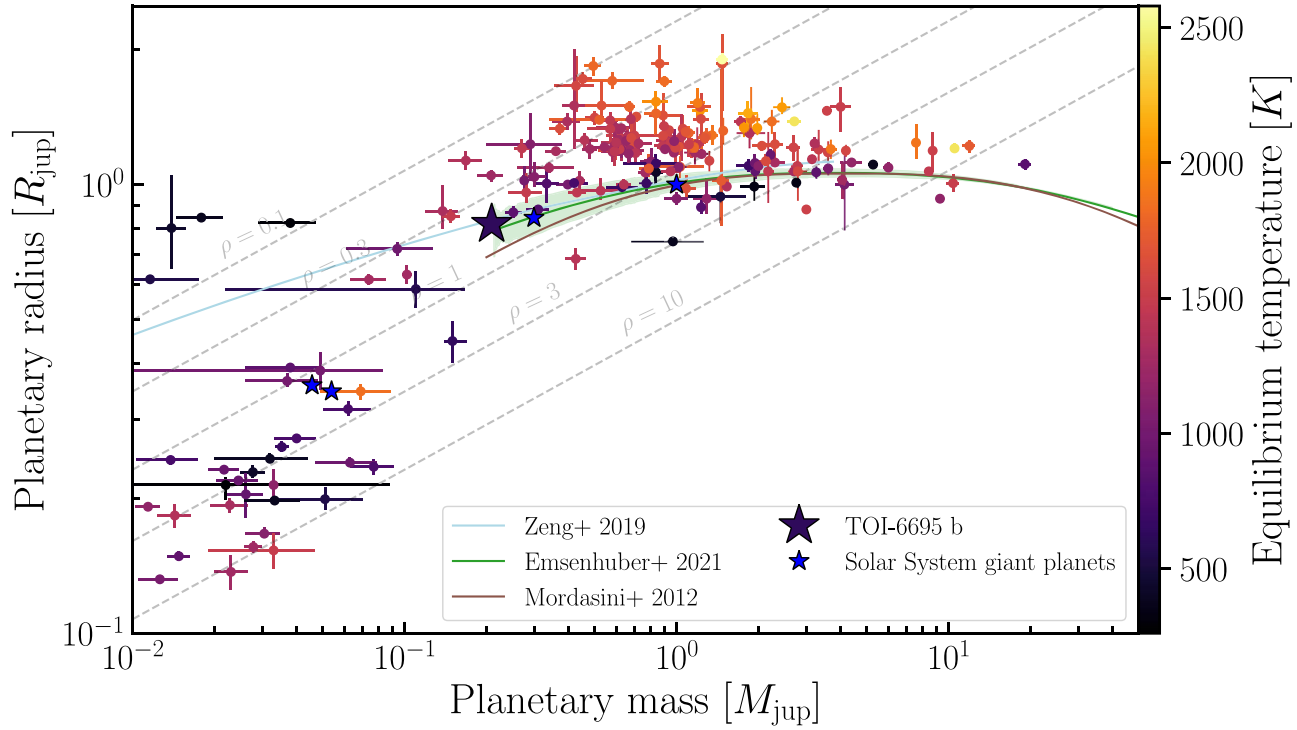

Figure 11. Mass–radius diagram for the same sample of planets as in Figures 9 and 10. Marked as blue star symbols are the solar system giant planets, whereas TOI-6695b is shown as a colored star symbol. Solid lines represent exoplanet composition models derived from the theoretical frameworks of C. Mordasini et al. (2012), L. Zeng et al. (2019), and A. Emsenhuber et al. (2021b). Dashed gray lines indicate fixed densities of $\rho = 0.1$, 0.3, 1.0, 3.0, and 1.0 g cm^{-3}. The shaded region surrounding the fit to the data from A. Emsenhuber et al. (2021b) illustrates the moving standard deviation of their synthetic planets, which arises from variations in core sizes and envelope metallicities (assumed to match stellar values).

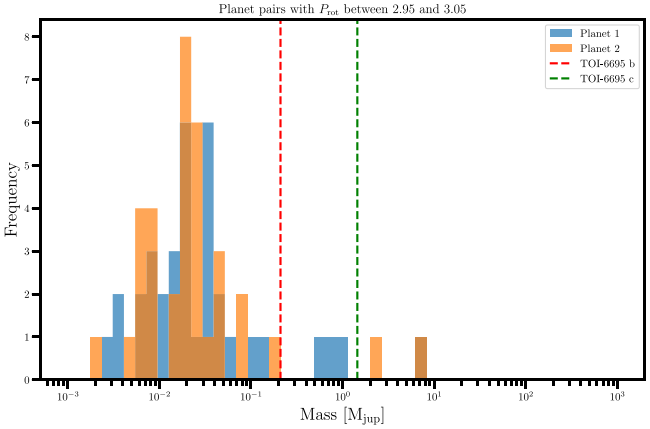

Figure 12. Mass distribution for planet pairs with a period ratio close to 3. The masses of TOI-6695b, and TOI-6695c are shown as dashed lines.

HD 60532b & c (J. Laskar & A. C. M. Correia 2009; A. J. Alves et al. 2016), as well as other systems close to the 3:1 MMR configuration without being in resonance, such as GJ 163 (X. Bonfils et al. 2013), HD 31527 (J. Pons & T. Gallardo 2024), TOI-560 (M. El Mufti et al. 2023), K2-254 (J. H. Livingston et al. 2018), Kepler-168, Kepler-180, Kepler-284, Kepler-359, Kepler-373 (J. F. Rowe et al. 2014), and Kepler-430 (M. E. Everett et al. 2015). Figure 12 shows the mass distribution of those 34 pairs of exoplanets. Most of the known planets among these 34 pairs are sub-Neptunes. TOI-6695b and c are among only a handful of giant planets in such a configuration. Similarly, this rarity is supported by simulations from A. Emsenhuber et al. (2021b) using a core accretion model of planet formation with disk evolution, N-body interactions, migration, and gas accretion (A. Emsenhuber et al. 2021a). Around Solar mass stars, four giant-planet ($M > 20\,M_{\oplus}$) pairs in 3:1 mean-motion resonances were obtained out of 1000 systems where 675 planets with masses above 20 Earth masses formed overall. For comparison, 34 pairs are close to a 2:1 mean-motion resonance, and two pairs close to 3:2. The resulting 3:1 pairs are visualized on a distance against mass diagram in Figure 13. As for the pair of planets around TOI-6695, the inner synthetic planet of the 3:1 period ratio pair is typically of lower mass than the outer. In the simulations, this is due to the inside-out opening of a gap in the gas disk (aided by planetary accretion itself), which first halts growth of the inner planets. In other words, owing to its position closer to the bulk of the disk gas mass, which is expected at around 30 au, the outer planet can accrete most of the gas accretion flux and prevent growth of the inner planet. Studying the dynamics and occurrences of resonantly coupled pairs of planets helps to understand the formation of planetary systems, and maybe even the formation of the solar system. According to the "Grand Tack" model (K. J. Walsh et al. 2011), Jupiter initially moved toward the Sun, until it reached a 2:3 resonance with Saturn, before reversing its migration (F. Masset & M. Snellgrove 2001) and moving together with Saturn away from the Sun again.

6. Summary

We report the discovery and characterization of a system of two giant exoplanets orbiting a Sun-like star. The inner planet, TOI-6695b was identified as a transiting planet candidate based on observations by TESS and later confirmed by RV follow-up observations with FEROS, HARPS, CHIRON, PFS, and

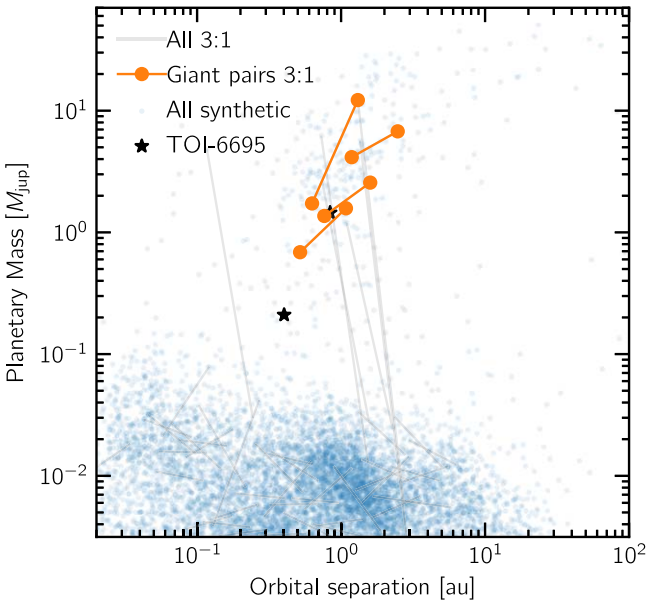

Figure 13. Mass-separation diagram for synthetic planets with neighboring planet pairs close to 3:1 mean-motion resonance marked. The data is drawn from the 50 embryo simulations of A. Emsenhuber et al. (2021b). Giant-planet pairs are found after excluding planets below 50 Earth masses from the systems.

CORALIE. Based on these RV observations, a second nontransiting planet, TOI-6695c has been identified. TOI-6695b is a Saturn-mass planet with a mass of $m_b = 0.21^{+0.01}_{-0.01}\,M_{\rm jup}$ and a planetary radius of $r_b = 0.85^{+0.02}_{-0.02}\,R_{\rm jup}$. It orbits the host star with an orbital period of ∼80.4 days on a low-eccentric orbit with an eccentricity of 0.04. Its bulk metal-mass fraction is about 0.3. TOI-6695c is a warm Jupiter with a minimum dynamical mass of $m_c = 1.45^{+0.03}_{-0.03}\,M_{\rm jup}$ orbiting its host star every 242 days on an orbit with an eccentricity of 0.022. The estimated equilibrium temperatures of TOI-6695b, and c are 599 ± 8 K and 415^{+5}_{-6} K, respectively. TOI-6695b and c are in a rare orbital configuration close to the 3:1 mean-motion resonance and are among the most massive planets of this extended subsample of Solar analogs.

Acknowledgments

This research has made use of the Exoplanet Follow-up Observation Program website, which is operated by the California Institute of Technology, under contract with the National Aeronautics and Space Administration under the Exoplanet Exploration Program. Resources supporting this work were provided by the NASA High-End Computing (HEC) Program through the NASA Advanced Supercomputing (NAS) Division at Ames Research Center for the production of the SPOC data products. We acknowledge the use of public TESS data from pipelines at the TESS Science Office and at the TESS Science Processing Operations Center. This paper includes data collected by the TESS mission, which are publicly available from the Mikulski Archive for Space Telescopes (MAST) operated by the Space Telescope Science Institute (STScI). Funding for the TESS mission is provided by NASA's Science Mission Directorate. T.T. acknowledges support by the BNSF program "VIHREN-2021" project No. KP-06-DV/5. R.B. acknowledges support from FONDECYT Project 1241963 and from ANID—Millennium Science Initiative—ICN12_009. R.Bu. acknowledges the financial support from DFG under Germany's Excellence Strategy EXC 2181/1-390900948, Exploratory project EP 8.4 (the Heidelberg STRUCTURES Excellence Cluster). The results reported herein benefitted from collaborations and/or information exchange within NASA's Nexus for Exoplanet System Science (NExSS) research coordination network sponsored by NASA's Science Mission Directorate under Agreement No. 80NSSC21K0593 for the program "Alien Earths." D.D. acknowledges support from the TESS Guest Investigator Program grant 80NSSC23K0769, and from the NASA Exoplanet Research Program grant 18-2XRP18_2-0136. M.T. P. acknowledges the support of Fondecyt-ANID fellowship no. 3210253 and ASTRON-0037. A.J. acknowledges support from ANID Millennium Science Initiative IM23-0001 and Fondecyt project 1251439.

Some of the observations in this paper made use of the NN-EXPLORE Exoplanet and Stellar Speckle Imager (NESSI). NESSI was funded by the NASA Exoplanet Exploration Program and the NASA Ames Research Center. NESSI was built at the Ames Research Center by Steve B. Howell, Nic Scott, Elliott P. Horch, and Emmett Quigley. This work made use of `tpfplotter` by J. Lillo-Box (publicly available at www.github.com/jlillo/tpfplotter), which also made use of the python packages `astropy`, `lightkurve`, `matplotlib` and `numpy`. This research has made use of `tglc`, which is available at https://github.com/TeHanHunter/TESS_Gaia_Light_Curve and is listed with doi:10.17909/610m-9474. The *TESS* data used for this analysis can be accessed via doi:10.17909/vwtg-p336. This work has been carried out within the framework of the NCCR PlanetS supported by the Swiss National Science Foundation under grants 51NF40_182901 and 51NF40_205606.

J.E. acknowledges the use of ChatGPT, which has been used on rare occasions for the purpose of rephrasing repetitive sentences. The outputs have been checked for their correctness and no original content has been created.

Facilities: *TESS*, El Sauce: 0.6m, Observatoire Moana, May Planck:2.2m, ESO:3.6 m, CTIO:1.5m, Magellan:Clay, Euler1.2m, WIYN.

Software: `Exo-Striker` (T. Trifonov 2019) `CERES` (R. Brahm et al. 2017a), `tesseract` (F. I. Rojas et al. 2025, in preparation.), `ZASPE` (R. Brahm et al. 2017b), `emcee` (D. Foreman-Mackey et al. 2013), `batman` (L. Kreidberg 2015), `TGLC` (T. Han & T. D. Brandt 2023), `ChatGPT` (OpenAI et al. 2023).

Appendix
Appendix Information

In this appendix, we present an additional figure and additional tables. Figure A1 shows a comparison between the transit of TOI-6695b in TESS sector 8 with the tesseract pipeline, Quick Look Pipeline and the Tess-Gaia-Light-Curve pipeline. Table A1 is a continuation of Table 2 and lists the relevant offset and jitter parameters for both the spectroscopic radial velocities and the photometric transit light curves. It also lists the quadratic limb-darkening coefficients for both the TESS and OMES light curves.

Tables A2, A3, A4, A5, and A6 list the radial velocity and stellar activity measurements for FEROS, HARPS, CHIRON, CORALIE, and PFS, along with their 1σ uncertainties.

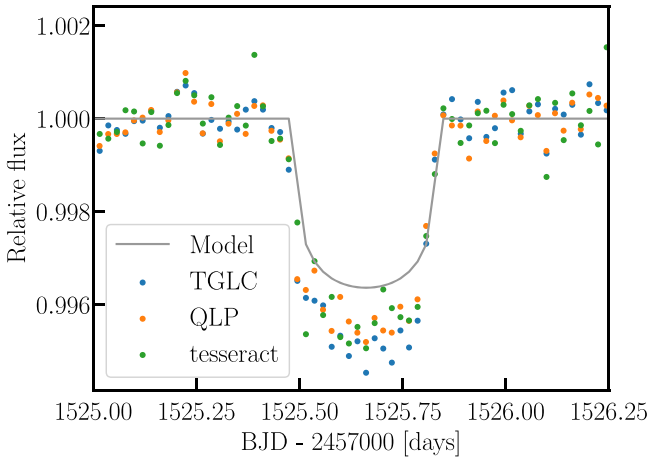

Figure A1. Transit of TOI-6695b in TESS sector 8 with the TGLC pipeline (`blue`), the QLP pipeline (`orange`) and the tesseract pipeline (`green`).

Table A1
Results from the Nested-sampling Run for TOI-6695

Parameter	Median and 1σ	Max. $-\ln\mathcal{L}$		Adopted Priors	
	Planet b	Planet c	Planet b	Planet c	Planet b	Planet c
$RV_{off.}$ HARPS [m s^{-1}]	…	$-33.4^{+0.6}_{-0.7}$	…	−33.4	…	$\mathcal{U}(-45, -15)$
$RV_{off.}$ CHIRON [m s^{-1}]	…	21498^{+2}_{-2}	…	21494	…	$\mathcal{U}(21470, 21530)$
$RV_{off.}$ PFS [m s^{-1}]	…	-4^{+1}_{-1}	…	−3	…	$\mathcal{U}(-20, 20)$
$RV_{off.}$ CORALIE [m s^{-1}]	…	135^{+2}_{-2}	…	134	…	$\mathcal{U}(100, 170)$
$RV_{jitt.}$ HARPS [m s^{-1}]	…	$5.9^{+0.4}_{-0.4}$	…	5.1	…	$\mathcal{U}(0.1, 20)$
$RV_{jitt.}$ CHIRON [m s^{-1}]	…	$4.5^{+0.7}_{-0.7}$	…	3.8	…	$\mathcal{U}(0.1, 20)$
$RV_{jitt.}$ PFS [m s^{-1}]	…	$5.0^{+0.6}_{-0.7}$	…	4.5	…	$\mathcal{U}(0.1, 20)$
$RV_{jitt.}$ CORALIE [m s^{-1}]	…	$2.6^{+0.5}_{-0.6}$	…	2.6	…	$\mathcal{U}(0.1, 20)$
$transit_{off.}$ T8	…	$0.00005^{+0.00002}_{-0.00002}$	…	0.00003	…	$\mathcal{U}(-0.001, 0.001)$
$transit_{off.}$ T34	…	$0.000094^{+0.000008}_{-0.000008}$	…	0.000097	…	$\mathcal{U}(-0.001, 0.001)$
$transit_{off.}$ T35	…	$0.000111^{+0.000007}_{-0.000007}$	…	0.000110	…	$\mathcal{U}(-0.001, 0.001)$
$transit_{off.}$ T61	…	$0.000090^{+0.000007}_{-0.000006}$	…	0.000092	…	$\mathcal{U}(-0.001, 0.001)$
$transit_{off.}$ OM-ES 1	…	$0.0010^{+0.0001}_{-0.0001}$	…	0.00098	…	$\mathcal{U}(-0.001, 0.001)$
$transit_{off.}$ OM-ES 2	…	$0.0008^{+0.0001}_{-0.0001}$	…	−0.0008	…	$\mathcal{U}(-1, 2)$
$transit_{jitt.}$ T8	…	$0.00030^{+0.00002}_{-0.00002}$	…	0.00028	…	$\mathcal{U}(0, 0.001)$
$transit_{jitt.}$ T34	…	$0.00017^{+0.00003}_{-0.00002}$	…	0.00011	…	$\mathcal{U}(0, 0.001)$
$transit_{jitt.}$ T35	…	$0.00017^{+0.00002}_{-0.00002}$	…	0.00017	…	$\mathcal{U}(0, 0.001)$
$transit_{jitt.}$ T61	…	$0.00017^{+0.00004}_{-0.00003}$	…	0.00015	…	$\mathcal{U}(0, 0.001)$
$transit_{jitt.}$ OM-ES 1	…	$0.0022^{+0.0002}_{-0.0002}$	…	0.0020	…	$\mathcal{U}(0, 0.003)$
$transit_{jitt.}$ OM-ES 2	…	$0.0001^{+0.0002}_{-0.0002}$	…	0.00008	…	$\mathcal{U}(-0.2, 0.2)$
u_1 TESS	…	$0.41^{+0.03}_{-0.04}$	…	0.31	…	$\mathcal{U}(0, 1)$
u_2 TESS	…	$0.39^{+0.11}_{-0.07}$	…	0.36	…	$\mathcal{U}(0, 1)$
u_1 OM-ES	…	$0.4^{+0.1}_{-0.1}$	…	0.3	…	$\mathcal{U}(0, 1)$
u_2 OM-ES	…	$0.26^{+0.06}_{-0.07}$	…	0.22	…	$\mathcal{U}(0, 1)$

Note. Listed are priors and posteriors for the RV and transit offsets and jitter parameters, as well as the quadratic limb-darkening coefficients. The orbital elements are in the Jacobi frame and are valid for epoch BJD = 2458400.0. The adopted priors are listed in the right-most columns and their meanings are $\mathcal{U}$—Uniform.

Table A2
FEROS Radial Velocity and Bisector Measurements, Along with their 1σ Uncertainties

BJD	RV ($m\,s^{-1}$)	σ_{RV}	BIS ($m\,s^{-1}$)	σ_{BIS}	Hα	$\sigma_{H\alpha}$	Ca II	$\sigma_{Ca\ II}$	S_MW	σ_{S_MW}	log RHK	$\sigma_{log\,RHK}$	Na II	$\sigma_{Na\ II}$	He I	$\sigma_{He\ I}$
2458909.692	209.3	13.2	30.0	12.0	0.117	0.003	0.116	0.009	0.144	0.011	−5.08	0.09	0.368	0.006	0.497	0.007
2458913.750	184.3	15.1	65.0	13.0	0.124	0.004	0.132	0.014	0.162	0.016	−4.95	0.10	0.380	0.007	0.500	0.008
2458917.775	130.3	11.5	−40.0	11.0	…	…	…	…	…	…	…	…	…	…	…	…
2458918.566	67.4	13.2	8.0	12.0	0.106	0.003	0.125	0.008	0.154	0.010	−5.00	0.07	0.362	0.006	0.494	0.007
2459188.770	158.8	9.3	33.0	10.0	0.101	0.002	0.126	0.004	0.155	0.007	−4.99	0.05	0.362	0.004	0.503	0.005
2459191.815	171.9	8.4	11.0	9.0	0.105	0.002	0.118	0.003	0.146	0.006	−5.06	0.05	0.378	0.003	0.500	0.004
2459206.765	157.8	9.4	65.0	10.0	0.108	0.002	0.116	0.004	0.144	0.006	−5.08	0.05	0.372	0.004	0.507	0.005
2459212.693	133.6	10.6	31.0	11.0	0.111	0.003	0.124	0.005	0.152	0.007	−5.01	0.05	0.374	0.005	0.509	0.006
2459578.779	117.4	10.4	48.0	11.0	…	…	…	…	…	…	…	…	…	…	…	…
2459579.760	121.9	12.8	44.0	12.0	0.106	0.003	0.136	0.008	0.166	0.010	−4.92	0.06	0.374	0.006	0.510	0.007
2459647.709	189.5	9.7	46.0	10.0	0.121	0.002	0.116	0.006	0.144	0.008	−5.08	0.07	0.387	0.004	0.498	0.005
2459652.727	150.9	9.7	−3.0	10.0	0.112	0.002	0.095	0.008	0.120	0.010	−5.34	0.15	0.371	0.004	0.500	0.005
2459655.777	70.8	14.7	−168.0	12.0	0.136	0.004	0.167	0.046	0.200	0.051	−4.75	0.21	0.385	0.007	0.510	0.008
2459681.680	175.8	11.5	44.0	11.0	0.114	0.002	0.111	0.025	0.138	0.028	−5.13	0.27	0.366	0.005	0.499	0.006
2459686.609	163.0	10.6	46.0	11.0	…	…	…	…	…	…	…	…	…	…	…	…
2459704.609	109.7	11.1	84.0	11.0	0.125	0.003	0.134	0.014	0.164	0.017	−4.93	0.10	0.358	0.005	0.511	0.006

Table A3.
HARPS Radial Velocity and Bisector Measurements Along with their 1σ Uncertainties

BJD	RV ($m\,s^{-1}$)	σ_{RV}	BIS ($m\,s^{-1}$)	σ_{BIS}	Hα	$\sigma_{H\alpha}$	log RHK	$\sigma_{\log RHK}$	FWHM	He I	$\sigma_{He\ I}$	Ca II	$\sigma_{Ca\ II}$	S_MW	σ_{S_MW}	Na II	$\sigma_{Na\ II}$
2458926.641	3.4	2.8	0.047	0.003	0.1033	0.0009	−5.48	0.13	10.082	0.502	0.002	0.085	0.003	0.113	0.006	0.395	0.002
2458930.660	6.5	5.8	0.032	0.009	0.1056	0.0020	⋯	⋯	10.063	0.502	0.005	0.009	0.009	0.031	0.011	0.389	0.004
2459178.862	−16.2	4.6	0.054	0.006	0.1051	0.0015	⋯	⋯	10.071	0.506	0.004	0.013	0.005	0.035	0.007	0.408	0.003
2459181.842	26.9	5.4	0.046	0.005	0.1065	0.0014	⋯	⋯	10.062	0.505	0.003	0.062	0.004	0.089	0.006	0.400	0.003
2459185.812	−17.0	4.1	0.044	0.005	0.1046	0.0014	⋯	⋯	10.048	0.502	0.003	0.059	0.004	0.085	0.006	0.405	0.003
2459190.699	−20.7	3.8	0.034	0.005	0.1028	0.0014	⋯	⋯	10.037	0.498	0.003	0.063	0.004	0.090	0.006	0.399	0.003
2459205.698	−32.2	4.4	0.041	0.005	0.1214	0.0015	⋯	⋯	10.107	0.501	0.003	0.043	0.004	0.068	0.006	0.406	0.003
2459213.715	−21.3	3.9	0.052	0.005	0.1021	0.0013	−5.62	0.19	10.051	0.501	0.003	0.080	0.004	0.107	0.006	0.403	0.003
2459213.729	−20.7	3.1	0.050	0.004	0.1019	0.0012	−5.34	0.10	10.063	0.501	0.003	0.092	0.004	0.121	0.006	0.401	0.003
2459227.799	−33.6	3.8	0.055	0.004	0.1040	0.0012	⋯	⋯	10.084	0.500	0.003	0.061	0.004	0.088	0.006	0.396	0.002
2459238.657	−37.4	4.3	0.040	0.006	0.1072	0.0017	⋯	⋯	10.071	0.490	0.004	0.052	0.005	0.078	0.007	0.393	0.003
2459247.710	−37.2	4.7	0.048	0.005	0.1029	0.0014	⋯	⋯	10.074	0.495	0.003	0.044	0.005	0.070	0.007	0.403	0.003
2459248.735	−52.7	3.3	0.040	0.004	0.1025	0.0011	−5.34	0.09	10.082	0.500	0.003	0.092	0.003	0.121	0.006	0.400	0.002
2459251.703	−50.0	4.4	0.034	0.005	0.1048	0.0014	⋯	⋯	10.120	0.497	0.003	0.059	0.005	0.085	0.007	0.409	0.003
2459254.665	−63.9	5.6	0.066	0.007	0.1038	0.0019	⋯	⋯	10.091	0.498	0.004	0.039	0.007	0.064	0.009	0.414	0.004
2459259.674	−73.9	3.0	0.056	0.005	0.1043	0.0013	⋯	⋯	10.092	0.496	0.003	0.046	0.004	0.071	0.007	0.396	0.003
2459263.707	−78.0	3.1	0.047	0.004	0.1033	0.0012	⋯	⋯	10.075	0.499	0.003	0.045	0.004	0.070	0.006	0.399	0.002
2459267.713	−82.4	3.8	0.036	0.005	0.1028	0.0014	⋯	⋯	10.051	0.503	0.003	0.049	0.005	0.075	0.007	0.408	0.003
2459296.652	−58.9	3.4	0.044	0.005	0.1043	0.0012	⋯	⋯	10.101	0.503	0.003	0.032	0.005	0.056	0.007	0.406	0.002
2459297.655	−51.2	3.8	0.025	0.006	0.1052	0.0015	⋯	⋯	10.062	0.501	0.003	0.032	0.006	0.056	0.008	0.413	0.003
2459365.476	−14.8	3.2	0.051	0.005	0.1049	0.0012	⋯	⋯	10.077	0.493	0.003	0.013	0.005	0.036	0.007	0.401	0.002
2459367.493	−8.7	4.0	0.024	0.006	0.1027	0.0013	⋯	⋯	10.024	0.496	0.003	0.006	0.006	0.028	0.008	0.397	0.003
2459368.495	−4.1	4.0	0.060	0.006	0.1036	0.0013	⋯	⋯	10.091	0.493	0.003	0.021	0.007	0.044	0.009	0.402	0.003
2459371.498	−9.5	3.6	0.068	0.005	0.1020	0.0012	⋯	⋯	10.062	0.498	0.003	0.044	0.007	0.069	0.009	0.400	0.002
2459504.855	−70.7	3.3	0.050	0.005	0.1035	0.0012	⋯	⋯	10.096	0.499	0.003	0.058	0.004	0.084	0.006	0.411	0.002
2459536.840	−61.0	2.1	0.037	0.003	0.1047	0.0009	⋯	⋯	10.070	0.500	0.002	0.083	0.002	0.111	0.005	0.399	0.002
2459563.772	−49.7	3.6	0.037	0.005	0.1074	0.0012	⋯	⋯	10.072	0.492	0.003	0.036	0.004	0.060	0.006	0.412	0.002
2459573.672	−52.4	2.9	0.032	0.004	0.1043	0.0011	⋯	⋯	10.065	0.496	0.003	0.066	0.003	0.093	0.006	0.399	0.002
2459573.805	−50.6	2.6	0.050	0.004	0.1033	0.0010	⋯	⋯	10.058	0.497	0.002	0.057	0.004	0.083	0.006	0.394	0.002
2459610.763	−11.8	2.9	0.049	0.003	0.1019	0.0010	⋯	⋯	10.066	0.495	0.002	0.066	0.003	0.092	0.006	0.391	0.002
2459620.714	4.6	2.9	0.045	0.003	0.1041	0.0009	−5.61	0.17	10.086	0.499	0.002	0.080	0.003	0.108	0.006	0.395	0.002
2459642.684	10.2	3.3	0.057	0.004	0.1028	0.0011	⋯	⋯	10.062	0.496	0.003	0.054	0.004	0.080	0.006	0.398	0.002
2459663.691	−4.4	3.4	0.044	0.005	0.1031	0.0011	⋯	⋯	10.083	0.497	0.003	0.065	0.005	0.092	0.007	0.397	0.002
2459668.657	−27.4	3.4	0.056	0.005	0.1029	0.0012	⋯	⋯	10.024	0.494	0.003	0.048	0.005	0.073	0.007	0.402	0.003
2459712.517	−38.8	4.2	0.044	0.006	0.1068	0.0013	⋯	⋯	10.080	0.493	0.003	0.032	0.006	0.056	0.008	0.405	0.003
2459723.503	−41.3	3.7	0.047	0.005	0.1045	0.0011	⋯	⋯	10.094	0.498	0.003	0.039	0.005	0.063	0.007	0.392	0.002
2459973.677	−59.5	3.3	0.042	0.004	0.1054	0.0011	⋯	⋯	10.071	0.498	0.003	0.042	0.003	0.066	0.006	0.404	0.002
2459977.673	−53.3	2.9	0.057	0.004	0.1047	0.0010	⋯	⋯	10.066	0.496	0.002	0.066	0.003	0.093	0.006	0.401	0.002
2460017.685	−64.7	3.2	0.036	0.004	0.1044	0.0010	⋯	⋯	10.085	0.501	0.002	0.045	0.003	0.070	0.005	0.394	0.002
2460035.539	−53.2	2.8	0.046	0.003	0.1057	0.0009	⋯	⋯	10.066	0.497	0.002	0.058	0.003	0.085	0.005	0.395	0.002
2460281.834	−49.9	3.5	0.046	0.006	0.1082	0.0014	⋯	⋯	10.027	0.501	0.003	0.043	0.004	0.068	0.006	0.401	0.003
2460293.811	−58.5	4.0	0.058	0.006	0.1070	0.0014	⋯	⋯	10.053	0.495	0.003	0.031	0.004	0.055	0.006	0.398	0.003
2460310.764	−50.8	2.9	0.064	0.004	0.1047	0.0010	⋯	⋯	10.068	0.498	0.003	0.064	0.003	0.091	0.005	0.391	0.002
2460328.742	−30.8	3.7	0.030	0.006	0.1056	0.0014	⋯	⋯	10.062	0.495	0.003	0.057	0.004	0.083	0.007	0.393	0.003
2460342.809	16.7	3.7	0.056	0.004	0.1054	0.0011	⋯	⋯	10.076	0.494	0.003	0.042	0.004	0.067	0.006	0.391	0.002
2460384.693	−4.7	3.0	0.047	0.003	0.1056	0.0010	⋯	⋯	10.096	0.495	0.003	0.052	0.004	0.077	0.006	0.392	0.002

Table A4
Processed CHIRON Radial Velocity and Bisector Measurements

BJD	RV ($m\ s^{-1}$)	σ_{RV}	BIS ($m\ s^{-1}$)	σ_{BIS}
2459185.837	21512.5	13.2	−44.0	25.0
2459193.827	21520.5	13.7	−15.0	17.0
2459200.793	21529.2	14.4	4.0	17.0
2459207.745	21516.1	14.9	19.0	19.0
2459213.793	21502.3	21.4	−2.0	22.0
2459222.755	21479.5	16.0	30.0	22.0
2459231.647	21486.4	11.9	55.0	20.0
2459238.726	21480.1	14.6	3.0	24.0
2459255.609	21444.1	10.2	39.0	19.0
2459260.754	21444.9	16.1	−6.0	28.0
2459268.676	21466.2	17.3	42.0	33.0
2459279.664	21462.0	12.5	21.0	28.0
2459285.708	21464.7	9.4	−13.0	34.0
2459290.695	21476.9	16.0	14.0	29.0
2459299.558	21488.7	13.5	42.0	28.0
2459349.520	21525.4	12.4	42.0	27.0
2459357.469	21552.3	19.9	63.0	26.0
2459364.484	21548.7	11.8	56.0	26.0
2459491.878	21502.5	43.1	134.0	49.0
2459535.828	21447.8	13.5	16.0	17.0
2459542.839	21476.2	15.3	26.0	16.0

Table A5
CORALIE Radial Velocity and Activity Measurements Along with their 1σ Uncertainties, Rounded to Significant Digits

BJD	RV ($m\,s^{-1}$)	σ_{RV}	FWHM ($m\,s^{-1}$)	σ_{FWHM}	BIS ($m\,s^{-1}$)	σ_{BIS}	Contrast	$\sigma_{contrast}$	H_α	σ_{H_α}	Na	σ_{Na}	Ca	σ_{Ca}	BERV	weight
2458868.867	139.1	26.3	10163.9	14.4	5.3	37.3	30.075935	0.000001	0.190	0.005	0.328	0.005	0.145	0.016	7.93	1
2458874.715	158.0	34.0	10143.2	14.3	16.9	48.1	30.412710	0.000001	0.200	0.006	0.321	0.006	0.173	0.019	5.96	1
2458881.749	139.7	22.2	10245.8	14.5	81.8	31.4	29.813853	0.000001	0.198	0.004	0.341	0.004	0.097	0.011	3.05	1
2458886.753	211.5	23.1	10233.4	14.5	10.5	32.6	29.662468	0.000001	0.191	0.005	0.346	0.004	0.048	0.011	1.02	1
2458900.580	186.8	24.4	10208.6	14.4	−25.5	34.6	29.817047	0.000001	0.193	0.005	0.336	0.005	0.093	0.013	−4.18	1
2458911.601	191.8	22.2	10178.3	14.4	−19.9	31.3	29.796913	0.000001	0.195	0.004	0.331	0.004	0.120	0.011	−8.49	1
2458917.554	190.9	26.0	10225.1	14.5	−84.9	36.8	29.431163	0.000001	0.196	0.005	0.333	0.005	0.186	0.013	−10.54	1
2458923.584	189.0	18.8	10157.4	14.4	21.8	26.6	29.581695	0.000001	0.188	0.004	0.324	0.004	0.156	0.009	−12.67	1
2459179.798	152.1	25.1	10165.3	14.4	43.0	35.5	30.089368	0.000001	0.208	0.005	0.333	0.005	0.092	0.013	22.41	1
2459183.792	177.3	19.3	10095.8	14.3	56.9	27.3	29.749666	0.000001	0.185	0.004	0.330	0.004	0.128	0.010	21.95	1
2459190.733	142.2	22.1	10243.0	14.5	162.2	31.3	29.821387	0.000001	0.190	0.005	0.344	0.005	0.111	0.012	21.01	1
2459622.765	176.4	14.0	10134.5	14.3	20.7	19.8	29.799852	0.000001	0.194	0.003	0.334	0.003	0.050	0.006	−1.25	1
2459637.720	158.7	13.9	10128.5	14.3	8.8	19.7	30.099597	0.000001	0.195	0.004	0.341	0.004	0.120	0.006	−7.09	1
2459642.596	194.6	12.4	10154.0	14.4	49.9	17.5	30.128359	0.000001	0.189	0.003	0.336	0.003	0.126	0.005	−8.66	1
2459687.593	131.6	13.0	10153.0	14.4	51.5	18.4	29.805901	0.000001	0.184	0.004	0.330	0.003	0.112	0.005	−21.00	1
2459700.540	143.0	14.0	10170.7	14.4	51.8	19.8	29.908795	0.000001	0.191	0.004	0.331	0.003	0.127	0.006	−22.36	1
2459711.541	126.9	14.7	10167.6	14.4	19.1	20.8	29.973974	0.000001	0.195	0.004	0.339	0.004	0.155	0.007	−22.72	1
2459726.548	116.3	15.1	10137.2	14.3	33.1	21.3	29.851747	0.000001	0.195	0.004	0.338	0.003	0.116	0.009	−21.99	1

Table A6
PFS Radial Velocity Along with their 1σ Uncertainties and Activity Measurements

BJD	RV ($m\ s^{-1}$)	σ_{RV}	S-index	Hα	counts	T_{exp}
2459205.721	0.00	2.46	−1.0000	0.02750	1506	900
2459205.732	−2.14	2.30	−1.0000	0.02724	1508	900
2459210.734	0.88	2.60	−1.0000	0.02739	1194	900
2459210.745	−3.81	2.55	−1.0000	0.02762	1347	900
2459215.754	0.97	2.56	−1.0000	0.02719	1249	900
2459215.765	9.81	2.53	−1.0000	0.02714	1197	900
2459238.731	−8.55	2.59	−1.0000	0.02723	1215	900
2459238.742	−7.95	2.46	−1.0000	0.02766	1416	900
2459358.471	13.76	2.35	−1.0000	0.02702	1785	1200
2459531.815	−46.48	2.86	−1.0000	0.02659	1365	1201
2459533.829	−43.48	2.56	−1.0000	0.02765	1924	1200
2459592.815	−3.48	2.33	−1.0000	0.02800	1764	1200
2459593.729	−3.70	2.71	−1.0000	0.02758	1135	1201
2459600.774	15.12	2.41	−1.0000	0.02781	1353	1200
2459601.783	12.77	2.43	−1.0000	0.02731	1447	1200
2459602.803	8.02	2.14	−1.0000	0.02757	1685	1200

ORCID iDs

Jan Eberhardt https://orcid.org/0000-0003-3130-2768
Trifon Trifonov https://orcid.org/0000-0002-0236-775X
Thomas Henning https://orcid.org/0000-0002-1493-300X
Marcelo Tala Pinto https://orcid.org/0009-0004-8891-4057
Rafael Brahm https://orcid.org/0000-0002-9158-7315
Andrés Jordán https://orcid.org/0000-0002-5389-3944
Nestor Espinoza https://orcid.org/0000-0001-9513-1449
Melissa J. Hobson https://orcid.org/0000-0002-5945-7975
Felipe I. Rojas https://orcid.org/0000-0003-3047-6272
Martin Schlecker https://orcid.org/0000-0001-8355-2107
Lorena Acuña https://orcid.org/0000-0002-9147-7925
Remo Burn https://orcid.org/0000-0002-9020-7309
Gavin Boyle https://orcid.org/0009-0009-2966-7507
Rodrigo Leiva https://orcid.org/0000-0002-6477-1360
James McCormac https://orcid.org/0000-0003-1631-4170
Diana Dragomir https://orcid.org/0000-0003-2313-467X
Jeffrey D. Crane https://orcid.org/0000-0002-5226-787X
Stephen Shectman https://orcid.org/0000-0002-8681-6136
Johanna K. Teske https://orcid.org/0009-0008-2801-5040
David Osip https://orcid.org/0000-0003-0412-9664
Arvind F. Gupta https://orcid.org/0000-0002-5463-9980
Solène Ulmer-Moll https://orcid.org/0000-0003-2417-7006
François Bouchy https://orcid.org/0000-0002-7613-393X
Monika Lendl https://orcid.org/0000-0001-9699-1459
Davide Gandolfi https://orcid.org/0000-0001-8627-9628
George R. Ricker https://orcid.org/0000-0003-2058-6662
Jon M. Jenkins https://orcid.org/0000-0002-4715-9460
Sara Seager https://orcid.org/0000-0002-6892-6948
Joshua N. Winn https://orcid.org/0000-0002-4265-047X

References

Acuña, L., Deleuil, M., Mousis, O., et al. 2021, A&A, 647, A53
Acuña, L., Kreidberg, L., Zhai, M., & Molliére, P. 2024, A&A, 688, A60
Albrecht, S. H., Dawson, R. I., & Winn, J. N. 2022, PASP, 134, 082001
Aller, A., Lillo-Box, J., Jones, D., Miranda, L. F., & Barcel Forteza, S. 2020, A&A, 635, A128
Alves, A. J., Michtchenko, T. A., & Tadeu dos Santos, M. 2016, CeMDA, 124, 311
Baluev, R. V. 2009, MNRAS, 395, 1541
Baranne, A., Queloz, D., Mayor, M., et al. 1996, A&AS, 119, 373
Beaulieu, J. P., Bennett, D. P., Fouque, P., et al. 2006, Natur, 439, 437
Boisse, I., Moutou, C., Vidal-Madjar, A., et al. 2009, A&A, 495, 959
Bonfils, X., Lo Curto, G., Correia, A. C. M., et al. 2013, A&A, 556, A110
Bozhilov, V., Antonova, D., Hobson, M. J., et al. 2023, ApJL, 946, L36
Brahm, R., Jordán, A., & Espinoza, N. 2017a, PASP, 129, 034002
Brahm, R., Jordán, A., Hartman, J., & Bakos, G. 2017b, MNRAS, 467, 971
Brahm, R., Espinoza, N., Jordán, A., et al. 2019, AJ, 158, 45
Brahm, R., Nielsen, L. D., Wittenmyer, R. A., et al. 2020, AJ, 160, 235
Butler, R. P., & Marcy, G. W. 1996, ApJL, 464, L153
Castelli, F., & Kurucz, R. L. 2004, in IAU Symp. 210, Modelling of Stellar Atmospheres, Poster Contributions, ed. N. Piskunov et al. (San Francisco, CA: ASP)
Charbonneau, D., Brown, T. M., Latham, D. W., & Mayor, M. 2000, ApJL, 529, L45
Crane, J. D., Shectman, S. A., & Butler, R. P. 2006, Proc. SPIE, 6269, 626931
Crane, J. D., Shectman, S. A., Butler, R. P., et al. 2010, Proc. SPIE, 7735, 773553
Crane, J. D., Shectman, S. A., Butler, R. P., Thompson, I. B., & Burley, G. S. 2008, Proc. SPIE, 7014, 701479
Dawson, R. I., & Johnson, J. A. 2018, ARA&A, 56, 175
Dawson, R. I., Huang, C. X., Brahm, R., et al. 2021, AJ, 161, 161
Duncan, D. K., Vaughan, A. H., Wilson, O. C., et al. 1991, ApJS, 76, 383
Eberhardt, J., Hobson, M. J., Henning, T., et al. 2023, AJ, 166, 271
El Mufti, M., Plavchan, P. P., Isaacson, H., et al. 2023, AJ, 165, 10
Emsenhuber, A., Mordasini, C., Burn, R., et al. 2021a, A&A, 656, A69
Emsenhuber, A., Mordasini, C., Burn, R., et al. 2021b, A&A, 656, A70
Espinoza, N., Kossakowski, D., & Brahm, R. 2019, MNRAS, 490, 2262
Espinoza, N., Brahm, R., Henning, T., et al. 2020, MNRAS, 491, 2982
Espinoza-Retamal, J. I., Brahm, R., Petrovich, C., et al. 2023, ApJL, 958, L20
Everett, M. E., Barclay, T., Ciardi, D. R., et al. 2015, AJ, 149, 55
Foreman-Mackey, D., Hogg, D. W., Lang, D., & Goodman, J. 2013, PASP, 125, 306
Gaia Collaboration 2020, yCat, I/350
Gaia Collaboration, Brown, A. G. A., Vallenari, A., et al. 2018, A&A, 616, A1
Gaia Collaboration, Vallenari, A., Brown, A. G. A., et al. 2023, A&A, 674, A1
Gomes da Silva, J., Santos, N. C., Bonfils, X., et al. 2011, A&A, 534, A30
Han, T., & Brandt, T. D. 2023, AJ, 165, 71
Henry, G. W., Marcy, G. W., Butler, R. P., & Vogt, S. S. 2000, ApJL, 529, L41
Hippke, M., David, T. J., Mulders, G. D., & Heller, R. 2019, AJ, 158, 143
Hippke, M., & Heller, R. 2019, A&A, 623, A39
Hobson, M. J., Brahm, R., Jordán, A., et al. 2021, AJ, 161, 235
Hobson, M. J., Trifonov, T., Henning, T., et al. 2023, AJ, 166, 201
Howell, S. B., Everett, M. E., Sherry, W., Horch, E., & Ciardi, D. R. 2011, AJ, 142, 19
Jenkins, J. M., Twicken, J. D., McCauliff, S., et al. 2016, Proc. SPIE, 9913, 99133E
Ji, J., Kinoshita, H., Liu, L., & Li, G. 2003, ApJL, 585, L139
Jones, M. I., Brahm, R., Espinoza, N., et al. 2019, A&A, 625, A16
Jones, M. I., Reinarz, Y., Brahm, R., et al. 2024, A&A, 683, A192
Jordn, A., Brahm, R., Espinoza, N., et al. 2020, AJ, 159, 145
Kaufer, A., Stahl, O., Tubbesing, S., et al. 1999, Msngr, 95, 8
Kossakowski, D., Espinoza, N., Brahm, R., et al. 2019, MNRAS, 490, 1094
Kreidberg, L. 2015, PASP, 127, 1161
Kunimoto, M., Huang, C., Tey, E., et al. 2021, RNAAS, 5, 234
Lagrange, A. M., Gratadour, D., Chauvin, G., et al. 2009, A&A, 493, L21
Laskar, J., & Correia, A. C. M. 2009, A&A, 496, L5
Lee, M. H., & Peale, S. J. 2003, ApJ, 592, 1201
Lehmann, C., Murphy, M. T., Liu, F., Flynn, C., & Berke, D. A. 2022, MNRAS, 512, 11
Livingston, J. H., Endl, M., Dai, F., et al. 2018, AJ, 156, 78
Marcy, G. W., & Butler, R. P. 1992, PASP, 104, 270
Masset, F., & Snellgrove, M. 2001, MNRAS, 320, L55
Mayor, M., Pepe, F., Queloz, D., et al. 2003, Msngr, 114, 20
Mayor, M., & Queloz, D. 1995, Natur, 378, 355
McLaughlin, D. B. 1924, ApJ, 60, 22
Mordasini, C., Alibert, Y., Georgy, C., et al. 2012, A&A, 547, A112
Noyes, R. W., Hartmann, L. W., Baliunas, S. L., Duncan, D. K., & Vaughan, A. H. 1984, ApJ, 279, 763
OpenAI, Achiam, J., Adler, S., et al. 2023, arXiv:2303.08774
Paegert, M., Stassun, K. G., Collins, K. A., et al. 2021, arXiv:2108.04778
Paredes, L. A., Henry, T. J., Quinn, S. N., et al. 2021, AJ, 162, 176
Pecaut, M. J., & Mamajek, E. E. 2013, ApJS, 208, 9
Pepe, F., Mayor, M., Rupprecht, G., et al. 2002, Msngr, 110, 9
Pons, J., & Gallardo, T. 2024, A&A, 685, A105
Queloz, D., Henry, G. W., Sivan, J. P., et al. 2001a, A&A, 379, 279
Queloz, D., Mayor, M., Udry, S., et al. 2001b, Msngr, 105, 1

Ricker, G. R., Winn, J. N., Vanderspek, R., et al. 2014, JATIS, 1, 014003
Rossiter, R. A. 1924, ApJ, 60, 15
Rowe, J. F., Bryson, S. T., Marcy, G. W., et al. 2014, ApJ, 784, 45
Schlecker, M., Kossakowski, D., Brahm, R., et al. 2020, AJ, 160, 275
Scott, N. J., Howell, S. B., Horch, E. P., & Everett, M. E. 2018, PASP, 130, 054502
Smith, J. C., Stumpe, M. C., Van Cleve, J. E., et al. 2012, PASP, 124, 1000
Southworth, J. 2011, MNRAS, 417, 2166
Speagle, J. S. 2020, MNRAS, 493, 3132
Stassun, K. G., Oelkers, R. J., Paegert, M., et al. 2019, AJ, 158, 138
Stumpe, M. C., Smith, J. C., Catanzarite, J. H., et al. 2014, PASP, 126, 100
Stumpe, M. C., Smith, J. C., Van Cleve, J. E., et al. 2012, PASP, 124, 985
Subasavage, J. P., Bailyn, C. D., Smith, R. C., et al. 2010, Proc. SPIE, 7737, 77371C
Tala Pinto, M., Jordán, A., Acuña, L., et al. 2025, A&A, 694, A268
Thorngren, D. P., Fortney, J. J., Murray-Clay, R. A., & Lopez, E. D. 2016, ApJ, 831, 64
Tokovinin, A., Fischer, D. A., Bonati, M., et al. 2013, PASP, 125, 1336
Trifonov, T., 2019 The Exo-Striker: Transit and Radial Velocity Interactive Fitting Tool for Orbital Analysis and N-body Simulations, Astrophysics Source Code Library, ascl:1906.004
Trifonov, T., Brahm, R., Espinoza, N., et al. 2021, AJ, 162, 283
Trifonov, T., Brahm, R., Jordán, A., et al. 2023, AJ, 165, 179
Vítková, M., Brahm, R., Trifonov, T., et al. 2025, ApJL, 978, L22
Walsh, K. J., Morbidelli, A., Raymond, S. N., O'Brien, D. P., & Mandell, A. M. 2011, Natur, 475, 206
Wisdom, J., & Holman, M. 1991, AJ, 102, 1528
Zechmeister, M., Dreizler, S., Ribas, I., et al. 2019, A&A, 627, A49
Zeng, L., Jacobsen, S. B., Sasselov, D. D., et al. 2019, PNAS, 116, 9723
Zhou, L.-Y., Lehto, H. J., Sun, Y.-S., & Zheng, J.-Q. 2004, MNRAS, 350, 1495